Doctoral Thesis

Design of Multifunctional Electrode-customized Separator Membrane for Lithium Metal Batteries

Yong-Hyeok Lee

School of Energy and Chemical Engineering
(Battery Science and Technology)

Ulsan National Institute of Science and Technology

2021

Design of Multifunctional Electrode-customized Separator Membrane for Lithium Metal Batteries

Yong-Hyeok Lee

School of Energy and Chemical Engineering
(Battery Science and Technology)

Ulsan National Institute of Science and Technology

Design of Multifunctional Electrode-customized Separator Membrane for Lithium Metal Batteries

A thesis/dissertation submitted to
Ulsan National Institute of Science and Technology
in partial fulfillment of the
requirements for the degree of
Doctor of Philosophy

Yong-Hyeok Lee

06.03.2021 of submission

Approved by

Advisor

Hyun-Wook Lee

Design of Multifunctional Electrode-customized Separator Membrane for Lithium Metal Batteries

Yong-Hyeok Lee

This certifies that the thesis/dissertation of Yong-Hyeok Lee is approved.

06.03.2021 of submission

Advisor: Hyun-Wook Lee

Sang-Young Lee

Youngsik Kim

Seok Ju Kang

Jae-Gyoung Gwon

Abstract

The forthcoming ubiquitous electronics era, which will find widespread use of the Internet of Things, flexible/wearable devices, and electric vehicles, has led to the pursuit of high-energy-density power sources with electrochemical sustainability. Among the numerous power sources reported to date, batteries have been widely used in various applications. discharging, and so on. The rational design and synthesis of major battery components such as anodes, cathodes, electrolytes, and separator membranes are essential for the development of high-performance batteries. Among other major battery components, separator membranes have not been the center of attention compared to other electrochemically active materials, despite their important roles in allowing ionic flow while preventing electrical contact between electrodes. Unfortunately, little attention was devoted to designing the separator membranes controlling the ion transport and functionality.

Most widely used separators are based on polyolefin (PE) materials. Although PE separators have many advantages, inhomogeneous porous structure (including low porosity, uneven pore-size, and local nonporous region) has been considered as limitations. To overcome the current limitations of separators, the novel designs of separators are needed. Most of all, it is important to develop the separators customized for each electrode (cathode and anode). Depending on the battery systems, new separator membranes are designed and classified as follows: 1) Cathode-customized separators for lithium-sulfur batteries and 2) Anode-customized separators for lithium-metal batteries. The proposed separator membranes can be suggested as promising strategies to outperform the current conventional separators.

Contents .....

List of Figures.....

List of Tables .....

Chapter Introduction

Chapter Overview of the Separators Approaches for Lithium Metal Battery

List of Figures

polysulfides (measured using the ICP analysis) trapped. Prior to this measurement, the separators were soaked in a model polysulfide solution.

Fig. 14 Amount of polysulfides (measured using the ICP analysis) trapped by: PIL vs. Al_2O_3. First, the PIL and Al_2O_3 were dipped into a polysulfides solution (5 mM Li_2S_6 in DOL/DME = 1/1 (v/v)) for 24 h.

Fig. 15 (a) UV-Vis spectra of polysulfides (Li_2S_6) solution depending on PIL concentration. (b) UV-Vis spectra: pristine electrolyte solution (1 M LiTFSI in DOL/DME = 1/1 (v/v), without poysulfides) vs. electrolyte solution containing the PIL with the trapped polysulfides.

Fig. 16 (a) Photographs showing color change of polysulfides (Li_2S_6) solution as a function of PIL and PVdF-HFP concentration. PIL and PVdF-HFP were respectively dipped into the polysulfide solutions and the color change of the solutions was monitored after 24 h. (b) Amount of polysulfides (measured using the ICP analysis) trapped by: VF nanomat vs. PE separator. (c) Variation of nitrogen content in the polysulfide solution containing the VF nanomat (or PE separator) as a function of time.

Fig. 17 (a) Amount of polysulfides (measured using the ICP analysis) trapped in VF-PE separator : at different discharge voltages of 2.15 and 1.50 V. (b) Charge/discharge profiles (1^{st} cycle) of the Li-S cells: assembled with the PE, VF-PE and VF-IC-PE separators. The sulfur cathode, Li metal anode and liquid electrolyte were used. The cells were charged/discharged at 0.5 C/0.5 C. (c) XPS S 2p spectra of VF-PE separator: 2.15 and 1.50 V.

Fig. 18 Fabrication of spiderweb separators and their application to Li-S batteries. (a) Schematic illustration depicting the stepwise fabrication process (bottom nanomat (PEI/MWCNT) → middle nanomat (PIL/PVdF-HFP) → top nanomat (PEI/MWCNT)) of the spiderweb separator, along with its photographs. The nanomats were fabricated through two nozzle-based dual electrospinning (or concurrent electrospinning/electrospraying) processes. (b) SEM images showing the surface of each layer of the spiderweb separator.

Fig. 19 Basic membrane characteristics of the spiderweb separator. (a) Nyquist plot of the spiderweb separator filled with liquid electrolyte. (b) Mechanical flexibility tests (tape test and crumpling deformation). (c) Amount of polysulfides trapped by the separators and (d) OCV profiles of the Li-S cells as a function of elapsed time (vs. PE separator).

Fig. 20 (a) Initial charge/discharging profiles of Li-S cells with the spiderweb and PE separators. The

sulfur cathode, Li metal anode and liquid electrolyte were used. The cells were cycled at 2.0 C/2.0 C. (b) Cycling performance (charge/discharge current density = 2.0 C/2.0 C) of the Li-S cells assembled with the spiderweb and PE separators.

Fig. 21 (a) Cycle performance (charge/discharge current density = 0.5 C/0.5 C) (areal sulfur loading = 4.5 mg cm^{-2}) assembled with the spiderweb separator. (b) SEM images of the spiderweb separator after 200 charge/discharge cycles at top nanomat (PEI/MWCNT) adjacent to the sulfur cathode.

Fig. 22 Changes in charge transfer resistance (R_{CT}) of the Li-S cells: with the spiderweb and PE separators depending on depth of discharge (DOD).

Fig. 23 Post-mortem analysis (after 200 cycles) of cells. (a) SEM image of the sulfur cathodes. (b) Polysulfides amount deposited on the lithium metal anodes. (c) XPS S 2p spectra of separator adjacent to the lithium metal anodes.

Fig. 24 Schematic illustration depicting the fabrication of CNC layer by vacuum-assisted self-assembly (VASA) and evaporation-induced self-assembly (EISA).

Fig. 25 (a) Polarized optical microscopy images of the CNC layer fabricated via EISA (vs. VASA (inset)). (b) Inclined-view cross-sectional SEM images of the CNC layer via EISA (vs. VASA (inset)). Photographs of (c) the CNC layer fabricated via EISA (vs. VASA (inset)). (d) different rotation angles.

Fig. 26 (a) Schematic illustration depicting the transfer of the cLC-CNC thin film to a Li metal foil using a roll-pressing process at room temperature. (b) Photographs of the cLC-CNC@Li before/after the taping test.

Fig. 27 (a) Schematic illustration depicting the transfer of the cLC-CNC thin film to a Li metal foil using a roll-pressing process at room temperature. (b) Photographs of the cLC-CNC@Li before/after the taping test.

Fig. 28 The COMSOL model domain with boundaries: (a) pristine metal, (b) VASA and (c) EISA CNC film.

Fig. 29 The COMSOL simulation results of Li-ion flux: (a) pristine metal, (b) VASA and (c) EISA CNC film.

Fig. 30 Suppressing Li dendrite growth by cLC-CNC skin. (a) A plot of the mechanical modulus of the cLC-CNC skin as a function of penetration depth during the nanoindentation test. (b) Unidirectional Li

plating profiles (at a current density of 0.35 mA cm^{-2}) and photographs (insets) of the pristine Li and cLC-CNC skin on Li. Morphological characterization of the Li metal with the cLC-CNC skin after the unidirectional Li plating for 72 h: (c) cross-sectional and (d) surface (pristine Li (inset)) SEM images. For the surface analysis, the cLC-CNC skin was pre-removed to exclusively observe the plated Li).

Fig. 31 Control of nanoporous structure of the cLC-CNC layer through pitch variation. (a) Schematic illustration depicting the dependence of pitch on the sonication time. (b)-(d) Structural change of the CNC layers as a function of sonication time (0, 1, and 2 h): (b) Cross-sectional SEM images, (c) UV-vis spectra, (d) Nyquist plots, and (e) Li plating/stripping profiles (at a current density of 0.35 mA cm^{-2} and a plating/stripping capacity of 1.75 mAh cm^{-2}).

Fig. 32 (a) Coulombic efficiency of the Li/Cu asymmetric cells (pristine Cu vs. cLC-CNC@Cu) at current density and a plating/stripping capacity (0.35 mA cm^{-2}, 1.00 mAh cm^{-2}. Voltage profiles of the Li/Cu asymmetric cells ((b) pristine Cu vs. (c) cLC-CNC@Cu) after 1st and 120th cycles.

Fig. 33 Effect of the cLC-CNC skin on Li plating/stripping. (a) Cross-sectional SEM image of pristine Li metal on Cu foil. (b) Li plating/stripping profiles (pristine Li vs. cLC-CNC@Li) at a current density of 0.35 mA cm^{-2} and 30 % DOD. (c) EIS analysis of the Li/Li symmetric cells after cycling test (460 h). Cross-sectional SEM images of (d) pristine Li and e) cLC-CNC@Li after the cycling test. (f) AFM images of the cLC-CNC@Li before and after the cycling test. (g) Polarized optical microscopy image of the cLC-CNC skin (cLC-CNC@Li) after the cycling test.

Fig. 34 Li plating/stripping profiles (pristine Li vs. cLC-CNC@Li) at a current density of 0.35 mA cm^{-2} and 50 % DOD.

Fig. 35 Photographs and SEM images of the PE separators facing the Li metal anodes after the cycling test (460 h) of symmetric cells: (a) pristine Li vs. (b) cLC-CNC@Li (pristine PE (inset)).

Fig. 36 Potential use of the cLC-CNC@Li for practical Li metal full cells. (a) Cycling performance of the Li metal full cell (composed of cLC-CNC@Li (vs. pristine Li) and NCM811 cathode (areal capacity = 1.6 mAh cm^{-2}, N/P ratio = 3.5) at charge/discharge current densities of 0.3 C/0.5 C. (b) Cycling performance of the Li metal full cell (composed of cLC-CNC@Li and NCM811 cathode (areal capacity = 3.8 mAh cm^{-2}, N/P ratio = 1.5) at charge/discharge current densities of 0.3 C/0.5 C. (c) Cross-sectional SEM images of the pristine Li (left) and cLC-CNC@Li (right) after 160 cycles. (d) Thickness increase (ΔT) of the Li metals and volumetric cell energy density retention after 160 cycles (pristine Li vs. cLC-CNC@Li). (e) Schematic illustration depicting the advantageous roles of cLC-CNC skin as a

List of Tables

Chapter I. Introduction

1.1 Overview of Rechargeable Battery Systems

Upcoming ubiquitous electronics era, which will find widespread use of the Internet of Things, flexible/wearable devices, and electric vehicles, has led to the pursuit of high-energy-density power sources with electrochemical sustainability.[1, 2] Among the numerous power sources reported to date, rechargeable battery including lithium-ion battery (LIB) has been widely used in various applications. A rechargeable battery comprised of two different electrodes such as cathode and anode, which is separated by electrochemically insulating porous separator membranes filling with ion conductive liquid electrolyte. The principle of rechargeable battery is based on redox reaction, i.e., oxidation and reduction, in each electrode. Electrons from oxidized electrode are forced to move to the other electrode through the external circuit, and simultaneously the electroneutrality is balanced by ion transport through electrolyte. In reversible process under the applying an external current, batteries are rechargeable. Most of all, it is important to design the proper redox couples in each electrode. The electrochemical capacity in electrodes is substantially affected by the number of electrons and molecular weight. Also, voltage of battery is decided by difference between potential of two electrodes involved. The increasing demands of batteries for requiring the energy density, power density, safety and cost. However, relative significance of each factor is depending on the application (Fig. 1).

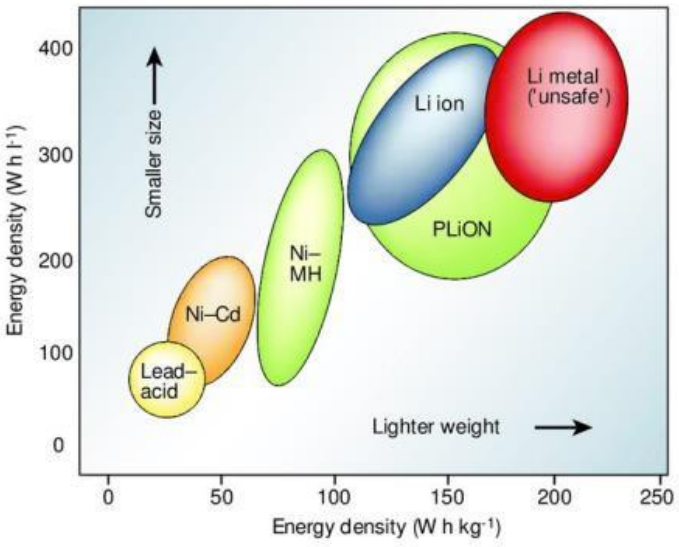

Fig. 1 Energy density of various battery systems.

1.2 Principles of Lithium-Ion Battery (LIB)

The lithium-ion battery (LIB) is a common rechargeable battery for portable electronics. LIBs consists of a positive and a negative electrode separated by an electrolyte solution containing dissociated salts, which enable ion transfer between the two electrodes. Since the first commercialization of $LiCoO_2$ cathode/Graphite system in SONY at 1991, LIB has still garnered great attention as promising power sources for various applications with a high energy density, high voltage window, long cyclability and eco-friendly operation.[3-5]

Once these electrodes are connected externally, the chemical reactions proceed in tandem at both electrodes, thereby liberating electrons and enabling the current to be tapped by the user. Both electrodes could store the Li ions to structure with process of intercalation and deintercalation. In discharge process, the Li ions transfer from anode (graphite, C_6) to cathode (e.g. Li metal oxide compounds, $LiCoO_2$) through electrolyte, while electrons move to cathode through external circuit. During charge, the reverse reaction occurs (Fig. 2). In LIB, the electrochemical reactions of electrodes are:

Cathode reaction (in $LiCoO_2$)

$$LiCoO_2 \rightleftharpoons Li_{1-x}CoO_2 + \ xLi^+ + xe^-$$

Anode reaction (in graphite)

$$xC_6 + xLi^+ + xe^- \rightleftharpoons xLiC_6$$

Overall cell reaction

$$LiCoO_2 + xC_6 \rightleftharpoons \ Li_{1-x}CoO_2 + xLiC_6$$

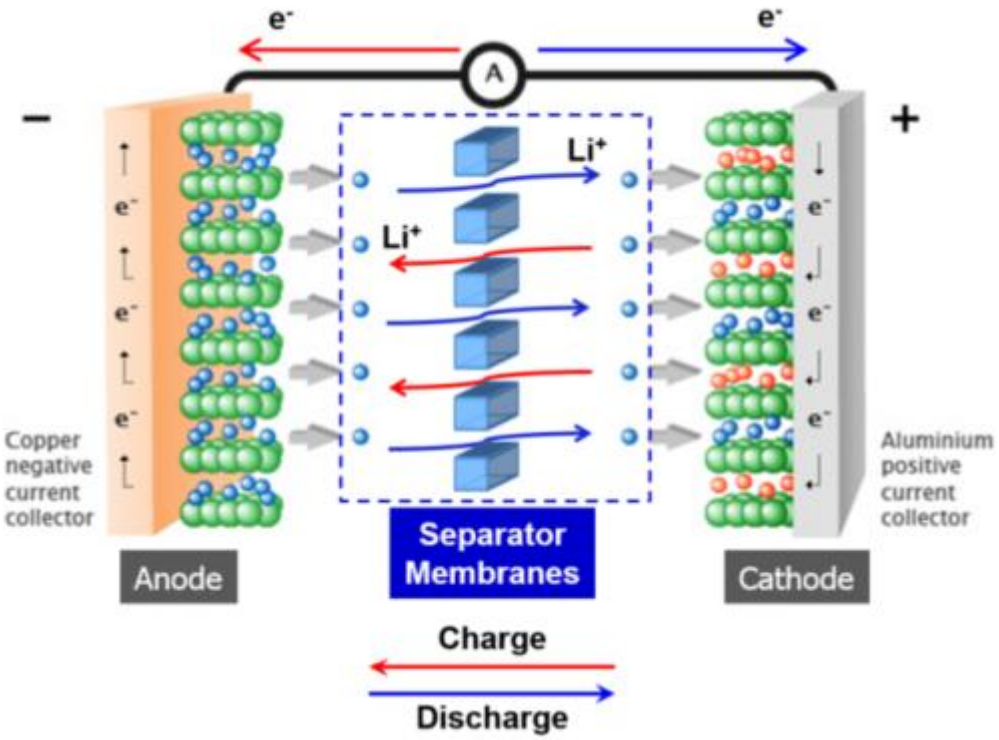

Fig. 2 Illustration of lithium-ion battery and charge/discharge reaction behavior

1.3 Needs for Battery Separators

Recently, the LIB suffers from potential risks such as volatilization, flammability and explosion. In result, the demands for safe LIB become strong. As increasing demands of safety, the role of separator, which is micrometer-scale insulating porous membrane, has become significant to secure the safety of battery. The separator membrane prevents the physical direct contact between electrodes, leading to the suppression of explosion. Also, for considering that the performance of battery could be determined by electron/ion transport, the separator membrane largely contribute to the battery performance. Therefore, a great deal of attention should be given to the separator membrane following reasons: 1) all ions for the Faradaic reaction of battery move through electrolyte-filled porous structure of separators and 2) internal short-circuit failure (which is major cause triggering cell fire or explosion) can be prevented.[6,7]

1.4 Requirements for Battery Separators

The importance of separators has been becoming critical in improving the electrochemical performance and safety. To apply the battery system, the separators should fulfill the basic requirements described below: 1) chemical and electrochemical stability against electrolyte and electrodes, 2) strong mechanical property to endure the penetration from electrodes, 3) sub-micrometer and uniform pore size, 4) optimal porosity for high ionic conductivity by holding sufficient amount of electrolyte, 5) homogeneous permeability leading to even current density distribution, 6) efficient wettability for electrolyte and 7) low thickness for high energy & power density with securing the safety.

Parameters	Target values	Unit	Test method
Sales price	< 1.00	US $	
Thickness	< 25	μm	ASTM D5947-96, ASTM D2103
Porosity	~ 40	%	ASTM D2873
Pore size	< 1	μm	ASTM 1294
Gurley value	~25	sec/100 cm^3	ASTM D726
Tensile strength	> 1000	kg/cm^2	ASTM D882
Puncture strength	> 300	g/mL	ASTM D3763
MacMullin number	< 8	-	N/A
Chemical stability	Long enough time	-	N/A
Thermal stability	< 5	% shrinkage	ASTM D1204
Melting point	> 150	°C	N/A
Skew	< 2	mm/m	N/A

Table. 1 General Specifications of Separators Announced by US Advanced Battery Consortium (USABC) (Zhang, S. S., J. Power Sources, 2007, 164, 351-364). Copyright © 2007 Elesevier.

1.5 Current Battery Separators

The most widely used separators in LIB are a kind of microporous polyolefin. Until now, the polyolefin separators have been applied to batteries due to its numerous advantages such as low cost, large productions and good accessibility. However, there are limitations for improvement of batteries, which is caused by the nonuniform distributed porous structure (including low porosity, uneven pore size, and partial nonporous region) and poor mechanical/thermal stability.

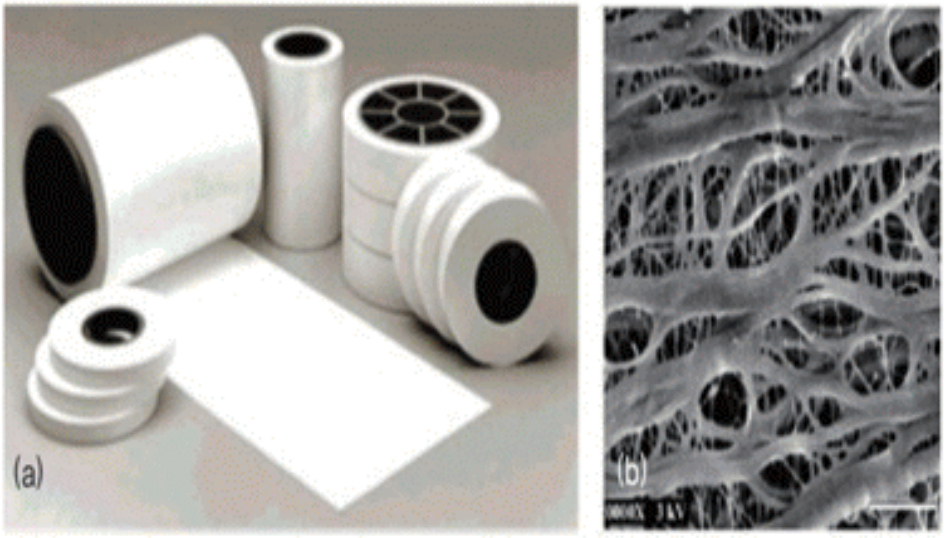

Fig. 3 Photo images (left) and SEM morphology (right) of commercial PE separator

1.6 References

1. S. Chu et al., *Nature*. **2012**. 488, 294-303.
2. W. Xu et al., *Energy Environ. Sci*. **2014**. 7, 513-537.
3. J. -M. Tarascon et al., *Nature*. **2001**, 414, 359-367.
4. J. B. Goodenough et al., *J. Am. Chem. Soc*. **2013**, 135, 1167-1176.
5. V. Etacheri et al., *Energy Environ. Sci.* **2011**, 4, 3243-3262.
6. P. Aroa et al., *Chem. Rev*. **2004**, 104, 4419-4462.
7. S. S. Zhang et al., *J. Power Sources.* **2007**, 164, 351-364.

Chapter II. Overview of the Separators Approaches for Lithium Metal Battery

2.1 Movements from Lithium-Ion Battery (LIB) to Lithium-Metal Battery (LMB)

It is true that the lithium-ion battery (LIB) has changed the modern life-style, making the portable electronics, electric vehicle and others possible. However, despite the appealing characteristics of LIB, the sluggish improvement of LIB for energy density give limitation for the increasing diverse applications.[1] The practical energy density of LIB has increased 6-fold in the past 150 years from the first-generation lead−acid batteries (~40 Wh kg^{-1}) to the present LIBs (~240 Wh·kg^{-1} and 640 Wh L^{-1}).

Therefore, to satisfy the demands for energy storage systems, advanced electrode becomes more attention for exceptional energy density. Among them, the Li metal battery, which is based on Li metal anode, has been regarded as promising material due to their extra-high capacity (3860 mAh g^{-1}), the lowest redox potential (-3.04 V vs standard hydrogen electrode) and low density. Also, LMB has been divided into diverse battery system depending on the cathode materials such as Li-O_2 and L-S battery. The energy density of LMB has been predicted to reach the high gravimetric and volumetric energy density (900-1900 Wh L-1 and 400-1000 Wh kg-1), which leads to longer driving distance over 400 miles per single charge and solving the limitation of LIB.[2]

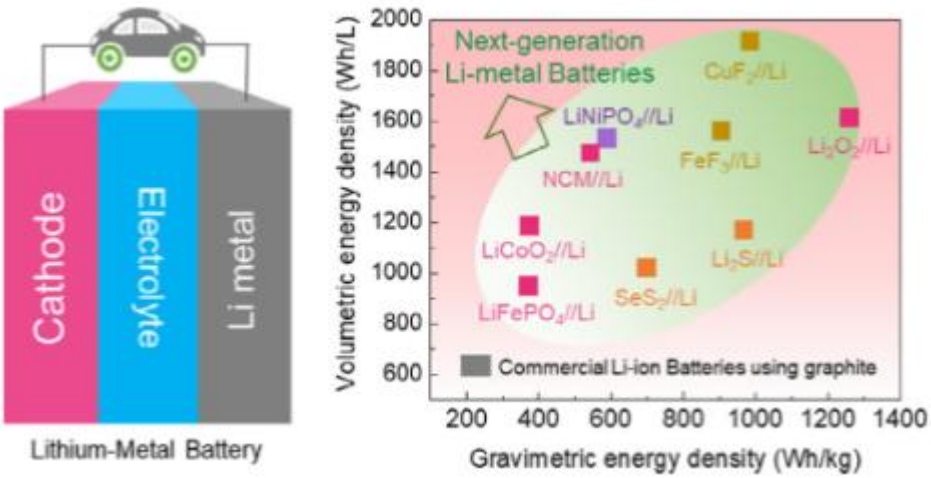

Fig. 4 Estimation of achievable energy density through LMB (R. Wang et al., *J. Energy Chem*. **2020**, 48. 145-159) Copyright © 2020 Elesevier

2.2 Issues of Lithium-Metal Battery (LMB)

Despite the attractiveness of Li metal anode, several technical challenges remain unsolved and has hindered their practical application. Li metal electrodes are still away from practical use due to their interfacial instability with electrolytes, formation of Li dendrites, uncontrolled volume changes, and generation of electrically inactive "dead Li". These challenges have forced the use of thick Li metal electrodes (> 100 μm) with low utilization (< 10 %), resulting in serious losses of cell energy density.[3,4]

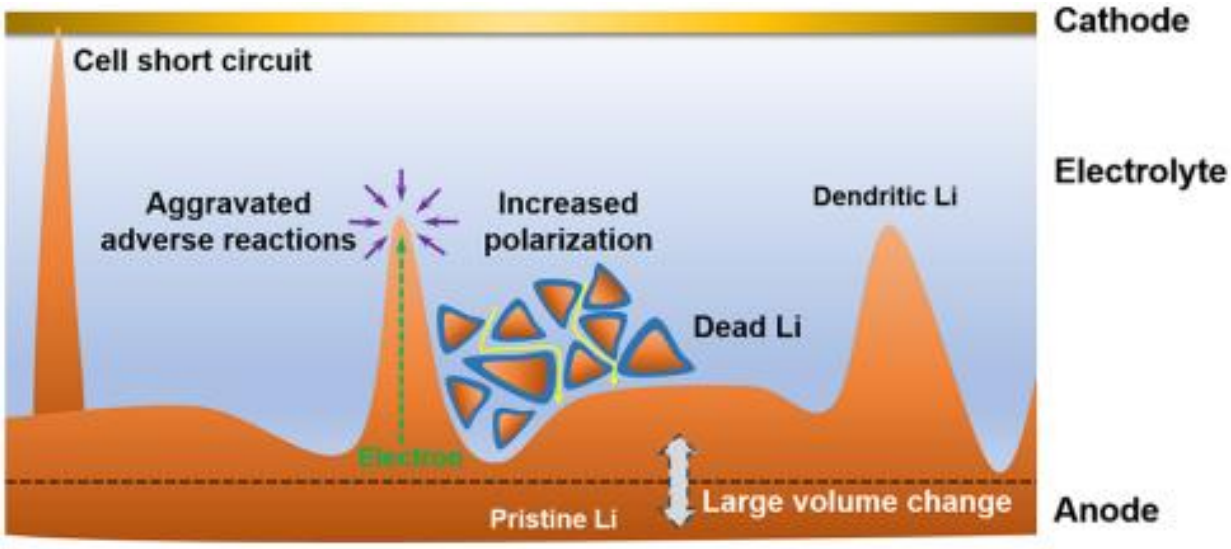

Fig. 5 Schematic issues of Li metal anode in LMB (Q. Zhang et al., *Chem. Rev.*, **2017**, 117, 10403-10473) Copyright © 2017 Royal Society Of Chemistry

2.3 Principles of Lithium-Sulfur Battery (LSB)

The energy density of conventional LIB has limitation to increasing demands of applications. Therefore, lithium-sulfur battery, which is the system based on sulfur-contained cathode and Li metal anode, have garnered much attention. Sulfur cathode is considered as promising electrode because of its high specific capacity (1675 mAh g^{-1}), energy density (2600 Wh kg^{-1}), and natural abundance.[5] In discharge process, the Li ions are released to the Li metal anode and transfer through electrolyte to cathode with passing through external circuit. Then, Li ions react to sulfur cathode and generate from soluble long chain polysulfides (Li_2S_8, Li_2S_6, Li_2S_4…) to insoluble short chain polysulfides (Li_2S_2, Li_2S) as final discharge products in cathode (Fig. 6).

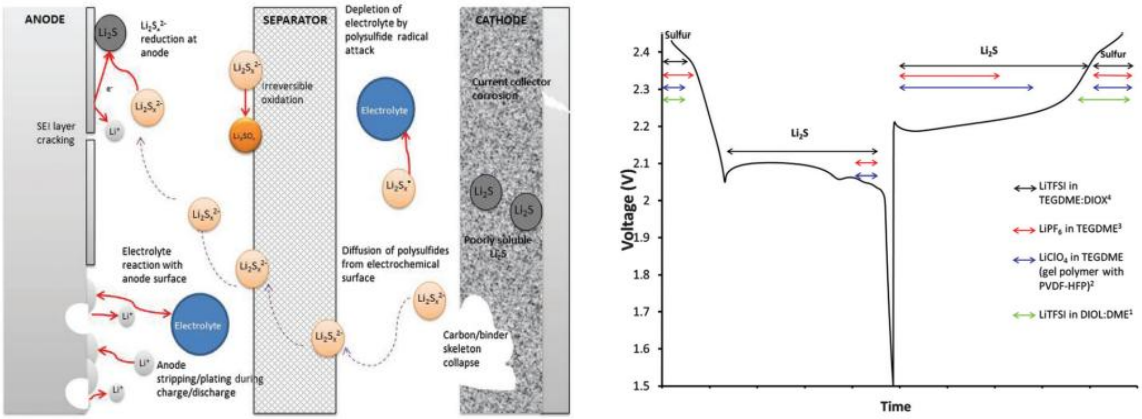

Fig. 6 Reaction mechanism and cell profile for LSB during charge/discharge process (M. Wild et al., *Energy Environ. Sci.*, **2015**, 8, 3477-3494) Copyright © 2015 Royal Society Of Chemistry

2.4 Issues of Lithium-sulfur battery (LSB)

Although LSB has the appealing characteristics, several technical challenges, such as the low electronic conductivity of sulfur/lithium polysulfide, structural instability of sulfur cathodes, unstable Li metal interface, and the shuttle effect of long-chain polysulfide, remain unsolved and has hindered their practical application. Most of all issues, the shuttle effect diffusing the long chain polysulfides to the Li metal anode and forming the irreversible short polysulfides on anode gives rise to cause degradation of cell performance (low coulombic efficiency, high internal resistance, capacity fade and self-discharge…) (Fig.7).

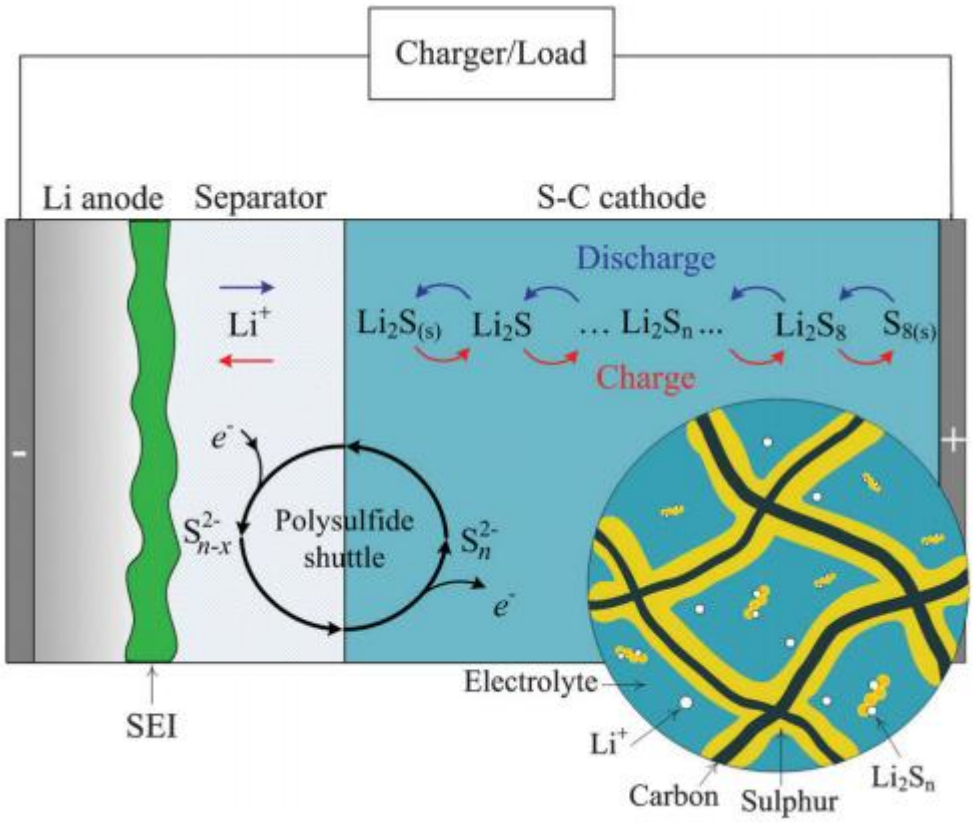

Fig. 7 Effects of polysulfides dissolution and shuttle effect (M. Wild et al., *Energy Environ. Sci.*, **2015**, 8, 3477-3494) Copyright © 2015 Royal Society Of Chemistry

2.5 Approaches

2.5.1 Separators for Lithium-Sulfur battery

Securing the functional separator has been considered as an effective approach to suppress the polysulfide shuttle effect and to improve the performance of Lithium–Sulfur battery. The strategies used for the prevention of polysulfide migration through the separator can be broadly classified into two classes: (1) Carbon-based material-coated separators, and (2) Non-carbon-based material-coated separators.

2.5.1.1 Carbon-based material-coated separators

Carbon-based coatings have been demonstrated to show excellent barrier properties against lithium polysulfides. Both physical trapping and chemical interactions with the lithium polysulfides can be achieved with carbon coatings. Also, it can facilitate the utilization of polysulfides captured within carbon-coated layer due to their high electronic conductivity. Commercially available and low-cost Super P carbon black was used to improve the battery performance of the PP separator. Li–S battery assembled with a carbon-coated PP separator and S cathode showed superior discharge performance. Figure 8 presents the carbon-coated separator that consists of a light-weight conductive carbon-coating on one side of a PP separator. Another carbon-based materials,[6,7] such as mesoporous carbon, graphene, carbon nanotube, are also introduced as the coating materials to the separator for Li-S batteries.

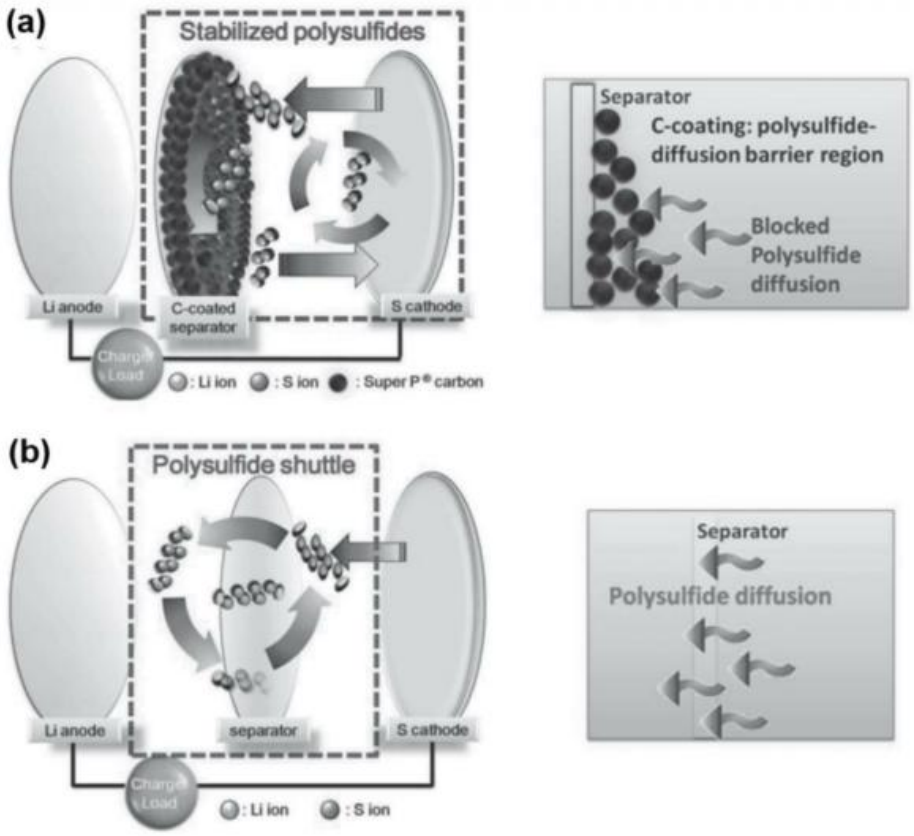

Fig. 8 Illustration working mechanism of (a) carbon-based coated separators and (b) commercial PP separator (A. Manthiram et al., *Adv. Funct. Mater*. **2014**, 24. 5299-5306) Copyright © 2014 John W iley & Sons, Inc

2.5.1.2 Non-Carbon-based material-coated separators

Metal oxide also can be used as a physical barrier to trap lithium polysulfides for the functionalization of separators in Li–S batteries. For example, Al_2O_3 coating was introduced on a polyolefin separator and good barrier properties were demonstrated with the battery tests.[8] MnO could also adsorb lithium polysulfides and a separator coated with MnO component had good battery performance.[9] Furthermore, MnO in the composite separator may contribute to the electrocatalytic reduction of lithium polysulfides, which further improves its battery performance. Montmorillonite (MMT) coatings can also improve the barrier properties of the polyolefin separators because of the electrostatic repulsion between MMT and lithium polysulfides in the electrolyte.

2.5.2 Separators for Lithium-Metal battery

Many researchers have studied the modification of electrolyte including design of add itives, high concentration electrolyte, solid electrolyte and others. However, considering the essential role which controls the ion current distribution through their porous structure contacting with anode, the modification of separator is also effective approaches for LMB. The separator approaches for LMB can be divided into 1) mechanical stabilization: mechanical suppression of Li dendrites, 2) physical stabilization: homogeneous Li ion flux through well-ordered porous structure and 3) chemical stabilization: uniform Li deposition through functionality.

2.5.2.1 Mechanical stabilization: mechanical suppression of Li dendrites

It is well-known that high mechanical modulus is required for separator to suppress dendrite propagation.[10] Because the modulus of Li dendrites is 4 GPa, the high modulus separators over 4 GPa has been developed for stabilization of Li metal anode. To increase the modulus of separators, the inorganic materials (Al_2O_3, ZrO_2, SiO_2…), polymers (polyethylene-oxide, polyacrylonitrile, polyimide…), graphene (graphene-oxide, reduced-graphene oxide…) and others are used to the separators.[11-13] These material-based separators showed the effective suppression of Li dendrites.

2.5.2.2 Physical stabilization: homogeneous Li ion flux through well-ordered porous structure

To lead the stabilization of Li ion flux, the well-ordered porous structure should be secured. This uniform Li ion flux produced the even Li ion deposition without Li dendrites. The well-ordered porous structure can divide the space into small and uniform confinements. Through small confinements, Li ions strongly tend to prefer the homogeneous transport along the ordered porous structure without any "hot-spots".

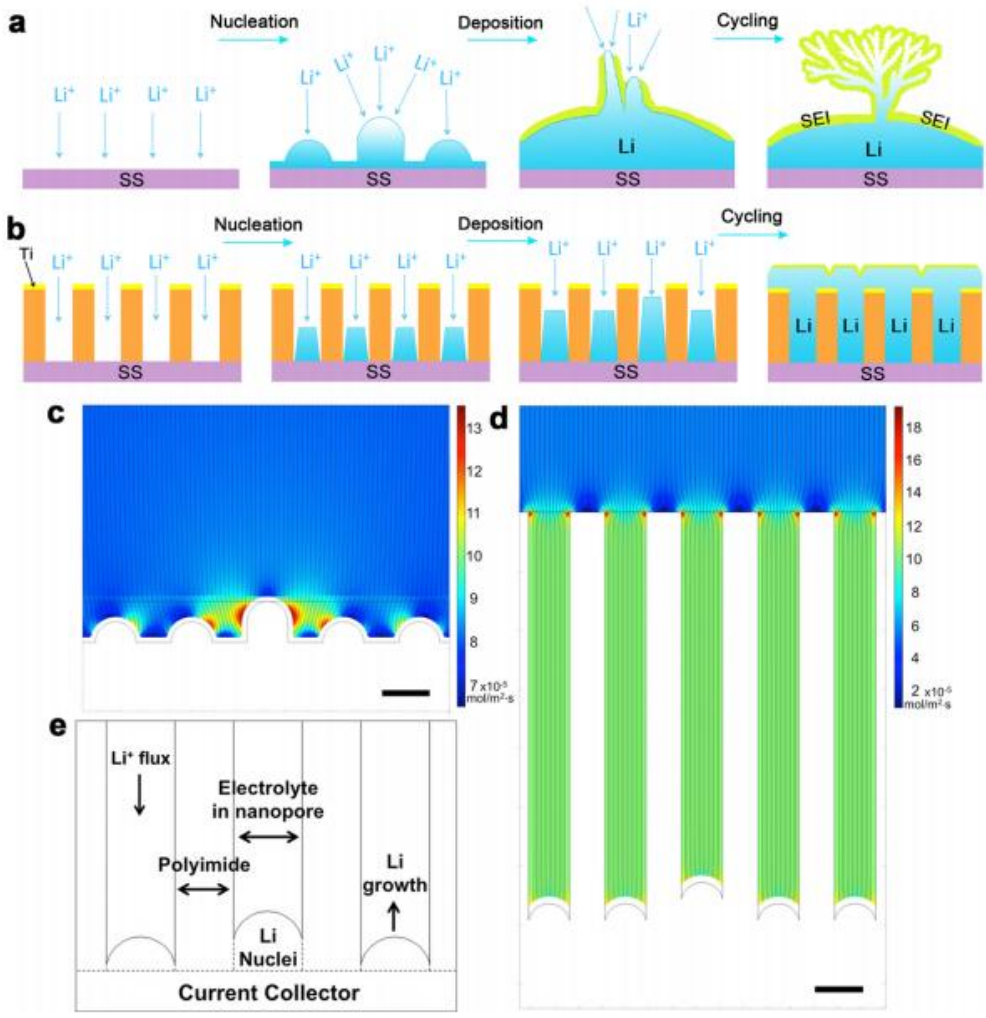

Fig. 9 Li ion flux with (a) bare separator and (b) vertical aligned nanochannel membrane. COMSOL simulation of Li ion flux for the (c) bare separator and (d) nanochannel membrane with e) cell geometry (Y. Cui et al., *J. Am. Chem. Soc.* **2016**, 138. 15443-15450) Copyright © 2016 American Chemical Society

2.5.2.3 Chemical stabilization: uniform Li deposition through functionality.

In addition to control of physical and mechanical properties, the chemical properties ع functionality can also play a critical role in bilization of Li metal anode. The functionality is largely classified with 1) cationic properties (for anion-trapping ability)[14, 15] and 2) anionic properties (for Lithiophilic ability)[16, 17]. The cationic functionality actively interacts with anions in the electrolyte and then selectively transfer the Li ions to Li metal anode by increasing Li ion transference number. In comparison, the anionic functionality has the Lithiophilic property which tends to attract the Li ions, leading to the uniform Li distribution through their functionality.

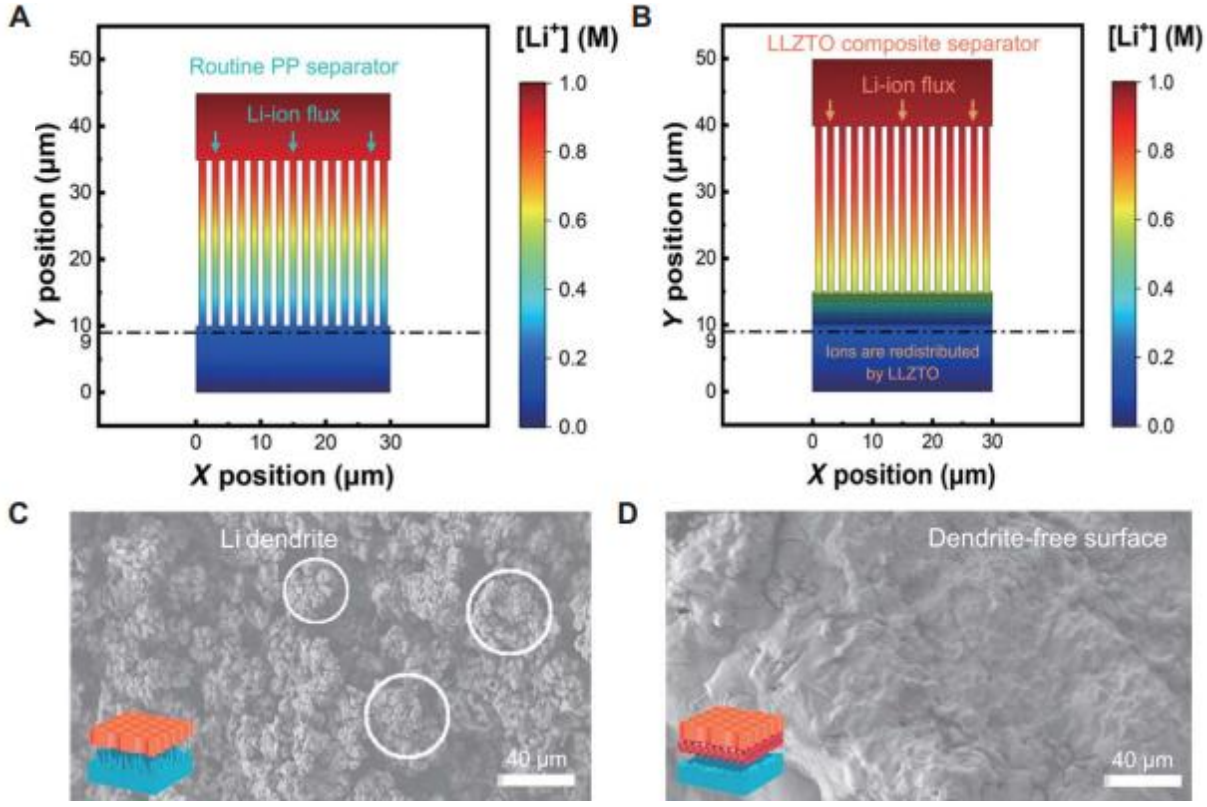

Fig. 10 Uniform Li deposition through Lithiophilic ability (Zhao. et. al., *Sci. Adv*. **2018**, 4, 3446.) Copyright © 2018 Science

2.6 References

1. Q. Zhang et al., *Chem. Rev*. **2017**, 117, 10403−10473
2. R. Wang et al., *J. Energy Chem.* **2020**, 48. 145-159
3. D. Lin et al. *Nat. Nanotech*. **2017**, 12, 194-206.
4. J. Alvarado et al., *Energy Environ. Sci*. **2019**, 12, 780-794.
5. A. Manthiram et al., *Chem. Rev*. **2014**, 114, 11751-11787.
6. J. Balach et. al., *Adv. Funct. Mater.* **2015**, 25, 5285-5291.
7. G. Zhou et. al., *Adv. Mater.* **2015**, 27, 641-647.
8. Zhang et. al., *Electrochim. Acta*. **2014**, 129, 55-61.
9. X. Qian et. al., Electrochim. Acta 2016, 192, 346-356.
10. Y. Liu et al., *Joule.* **2018**, 2, 1595-1609.
11. Y. Cui et al., *Adv. Mater.* **2017**, 29, 1605531.
12. R. Pathak et al., *Nat. Commun*. **2020**, 11, 1-10.
13. A. C. Kozen, et al., *ACS Nano*. **2015**, 9, 5884-5892.
14. J. C. Lee et. al., *ACS Appl. Mater. Interfaces*. **2016**, 8, 27740-27752.
15. S. Y. Lee et. al., *Adv. Funct. Mater*. **2021**, 30, 2000792.
16. Chen. et. al., *Nat. Commun*. **2019**, 10, 4973.
17. Zhao. et. al., *Sci. Adv*. **2018**, 4, 3446.

Chapter III. Cathode-customized Functional Separators for Lithium-Sulfur Battery

3.1 Introduction

Forthcoming smart energy era has pushed us to develop high energy density power sources.[1-3] Lithium-sulfur (Li-S) batteries[4-10] garnered considerable attention as a promising system over the current Li-ion batteries. Li-S batteries show a high theoretical capacity (1672 mAh g^{-1}), low cost, natural abundance and use of environmentally benign sulfur active materials. Despite such remarkable advantages, the practical use of Li-S batteries is challenging due to the electrically inert nature of sulfur, the volume change of sulfur cathodes and the shuttle effect of lithium polysulfides (PS) (Li_2S_x).[11-13] Shuttle effect and accumulation of irreversible low-order lithium PS (including Li_2S_2 and Li_2S) on electrodes. And it is considered as formidable obstacles for long-term performance.

Enormous research efforts have been undertaken.[14-19] Meanwhile, considering that all ions (including PS) in electrolytes move through electrolyte-soaked separators between the sulfur cathodes and Li metal anodes, separators should not be underestimated in research activities on preventing the shuttle effect. Recently, the modification of separators with carbon-based conductive layers[20-28] and the introduction of multilayered separators[29,30] were extensively investigated to suppress the shuttle effect and to facilitate the electrochemical reaction kinetics of sulfur cathodes. Another noteworthy separator-based approach relies on the "Donnan Exclusion" of polyelectrolyte membranes such as Nafion or other cation-conducting membranes.[31-35] Due to the anion (e.g., sulfonate (SO_z^-) or carboxyl (COO^-)) groups of the polyelectrolyte membranes, the membranes can repel polysulfides that intrinsically possess anionic characteristics. However, ion transport through polyelectrolyte membranes is sluggish compared to that of conventional porous separators, resulting in the unsatisfactory electrochemical performance (e.g., large overpotential problems) of the resultant Li-S batteries. Recently, to compensate the drawbacks of single composite, the trilayered separators with multicomponents were developed, resulting in the more improved suppression of polysulfide shuttle effect and sulfur utilization than one functional layer.

Nazar[36,37] and Lee[38] reported the reversible adsorption/desorption of polysulfides by SBA-15 (used as a sulfur cathode component) and MCM-41 (an interlayer component) particles as a function of depth of discharge (DOD), which effectively alleviated capacity decay with cycling. Here, intrigued by these interesting phenomena, we demonstrate a new class of spiderweb-mimic, anion-exchangeable separators based on polyionic liquids (denoted as "spiderweb separators") as a membrane approach to address the aforementioned challenges of Li-S batteries. Poly(1-ethyl-3-methylimidazolium)

bis(trifluoromethanesulfonyl)imide (PVIm[TFSI]) was rationally synthesized as a model polyionic liquid to explore the feasibility of this concept. Due to polysulfide concentration gradient-driven diffusion during the charge/discharge reaction, the TFSI- anions of the PVIm[TFSI] are expected to reversibly undergo an anion exchange reaction with soluble polysulfides.

The spiderweb separator is composed of sandwich-type, three functional nanomats (top and bottom layers = multi-walled carbon nanotube (MWCNT)-wrapped polyetherimide (PEI) nanomats, middle layer = PVIm[TFSI]/poly(vinylidene fluoride-co-hexafluoropropylene) (PVdF-HFP) nanomat) on top of a porous polyethylene (PE) separator. The three nanomat layers of the spiderweb separator are fabricated through two nozzle-based, dual electrospinning (or concurrent electrospinning/electrospraying) processes. The middle nanomat layer (PVIm[TFSI]/PVdF-HFP) is rationally designed to show a spiderweb-mimic porous morphology. Note that the anion-exchangeable PVIm[TFSI] nanofibers are highly reticulated between the PVdF-HFP nanofibers serving as a mechanical skeleton. Meanwhile, the top and bottom nanomat layers (PEI/MWCNT) act as an upper current collector (the top nanomat: adjacent to the sulfur cathodes) to boost the electrochemical redox reaction of the sulfur cathodes and a blocking layer (the bottom nanomat: facing the PE separator) to prevent crossover of the polysulfides to the Li metal anodes, respectively.

Benefiting from the structural uniqueness and chemical functionalities that have never been reported in Li-S battery separators, the spiderweb separator significantly suppresses the shuttle effect while ensuring facile Li ion transport, eventually providing exceptional improvement in the electrochemical performance (in particular, charge/discharge capacity retention with cycling) of Li-S batteries.

3.2 Experimental Section

3.2.1 Synthesis of PVIm[TFSI] (PIL)

The PVIm[TFSI] (polyionic liquid, PIL) of the spider separator was synthesized.[39-41] First, 1-vinylimidazole was mixed with bromoethane in chloroform for 1 h to obtain the 1-vinyl-3-ethylimidazolium bromide ([VIm^+][Br^-]) monomer. Then, the [VIm^+][Br^-] monomer was polymerized at 60 ^oC for 2 h in the presence of 2 % azobisisobutyronitrile (AIBN) as an initiator to yield poly[VIm^+][Br^-]. Finally, excess LiTFSI was added into the obtained poly[VIm^+][Br^-] solution to allow anion exchange reaction between Br^- and $TFSI^-$ anions, resulting in PVIm[TFSI].

PVIm[TFSI] was synthesized through a radical polymerization (Figure 11a, (i)).[39-41] The chemical structure of the obtained PVIm[TFSI] was identified using FT-IR spectra (Figure 11b). The ion exchange capacity (IEC) value of the PVIm[TFSI] was quantitatively measured using a titration method (ASTM D2187). Details on the measurement were described in the experimental section. The obtained IEC value of the PVIm[TFSI] was 1.21 mmol g^{-1}. To verify the anion exchange reaction of PVIm[TFSI] with the polysulfides (schematically shown in Figure 11a, (ii)), a supplementary experiment was conducted.

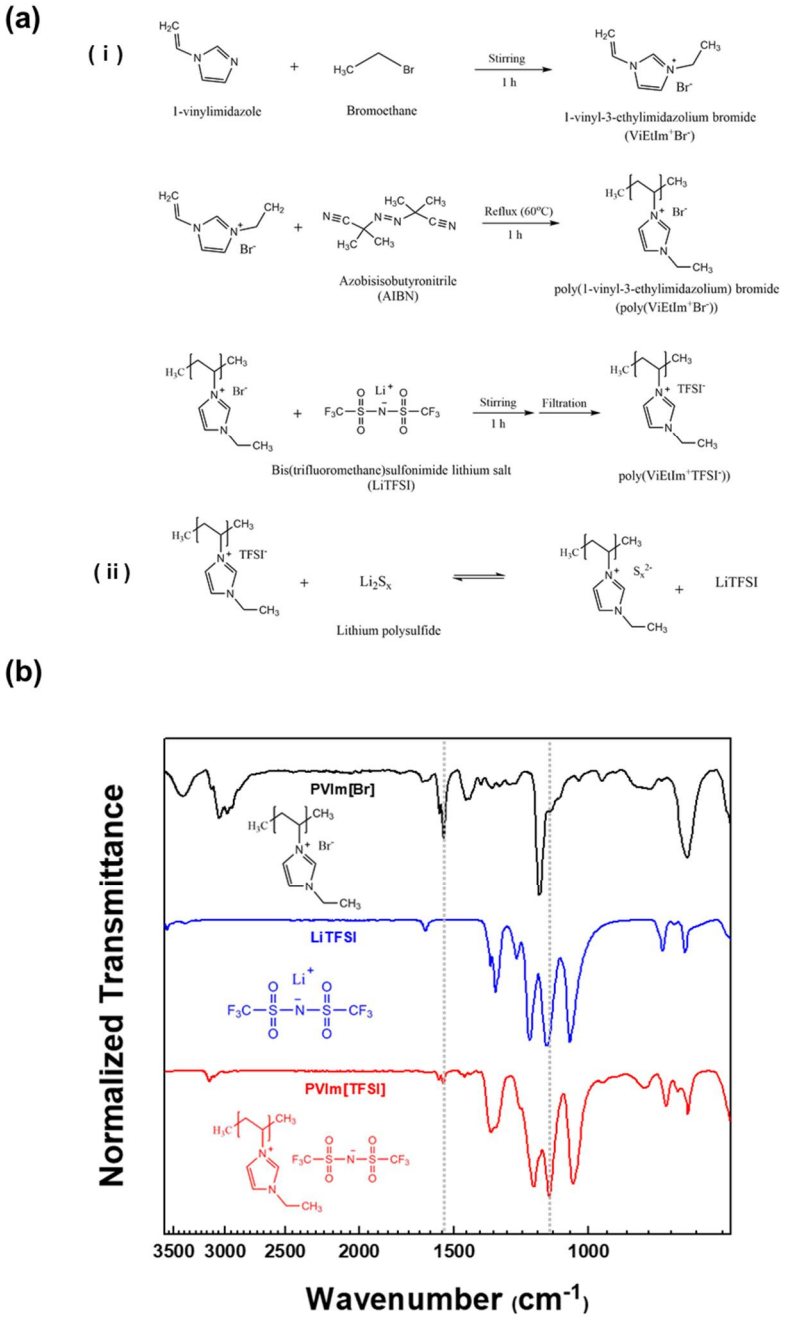

Fig. 11 (a) (i) Synthetic scheme of PIL. (ii) anion exchange reaction between $TFSI^-$ (from PIL) and polysulfides. (b) FT-IR spectra of the synthesized PIL. The characteristic peaks assigned to PVIm cations and TFSI anions were marked by symbols of + and *, respectively.

3.2.2 Fabrication of PVIm[TFSI]/PVdF-HFP-based nanomat (VF nanomat)

To fabricate the top and bottom layers (*i.e.*, PEI/MWCNT nanomats), 25 wt% PEI (Ultem 100) was dissolved in DMAc/NMP = 1/1 (w/w) at 70 °C for 12 h. The MWNTs (average length = 1.5 μm, diameter 9.5 nm from NANOCYL (Belgium)) were ultrasonicated for 1 h in water/IPA = 70/30 (w/w) with 10 % PVP (molecular weight = 150,000 g mol^{-1}, Aldrich) as a dispersing additive for the MWCNTs. The bottom layer (PEI/MWCNT nanomat) was deposited on the PE separator via concurrent electrospinning (for PEI)/electrospraying (for MWCNTs) followed by hot-roll pressing at 90 °C. The detailed experimental conditions were 9.0 kV with a feed rate of 3 μL min^{-1} (for electrospinning) and 15 kV with a feed rate of 65 μL min^{-1} (for electrospraying). Subsequently, to fabricate a middle layer (*i.e.*, PVIm[TFSI]/PVdF-HFP nanomat), 25 wt% PVdF-HFP and 30 wt% PVIm[TFSI] were dissolved in DMF/acetone = 7/3 (w/w), respectively. The PVdF-HFP and PVIm[TFSI] solutions were independently electrospun through two different nozzles on top of the above-prepared bottom layer (PEI/MWCNT nanomat)-deposited PE separator. Finally, the obtained middle/bottom layers-deposited PE separator was laminated with a top layer (PEI/MWCNT nanomat) using a roll-pressing method (at room temperature), eventually producing the spiderweb separator (*i.e.*, sandwich-type, three functional nanomats (top (3 μm)/bottom (3 μm) layers = PEI/MWCNT nanomats, middle layer (6 μm) = PVIm[TFSI]/PVdF-HFP nanomat) on the PE separator (thickness = 20 μm)).

The PVIm[TFSI] solution (solvent = dimethylacetamide (DMF)/acetone = 7/3 (w/w)) was subjected to a single nozzle-based electrospinning, which failed to produce a self-standing film with a reliable mechanical strength (inset of Figure 12a). To resolve this problem, PVdF-HFP (as a mechanical skeleton) was combined with PVIm[TFSI]. The PVIm[TFSI] and PVdF-HFP solutions were independently electrospun through two different nozzles, to yield a self-standing nanomat with a thickness of 6 μm (Figure 12a). The composition ratio of the PVIm[TFSI]/PVdF-HFP nanomat was estimated to be 25/75 (w/w) by measuring its weight change after the selective removal of PVIm[TFSI] using IPA as a solvent. Figure 12b shows that the fabricated PVIm[TFSI]/PVdF-HFP nanomat has a spiderweb-mimic, highly reticulated porous structure in which the straightforward/thick fibers correspond to the PVdF-HFP and the relatively crooked/thin fibers are ascribed to the PVIm[TFSI]. As supplementary evidence, the porous morphologies of the bare PVdF-HFP and PVIm[TFSI] nanomats themselves are provided (left of Figure 12b). Note that the spiderweb-mimic, porous morphology of the nanomat was affected by the PVIm[TFSI] concentration. The relatively low PVIm[TFSI] concentration (*e.g.*, 10 wt%) led to the formation of a poorly developed spiderweb-mimic morphology in comparison to that with PVIm[TFSI] concentration of 30 wt% (shown in Figure 12b). At a PVIm[TFSI]

concentration above 30 wt%, the polymer solution was not suitable for the electrospinning process because of its excessively high viscosity (*e.g.*, 8386 cP at 35 wt% PVIm[TFSI]).

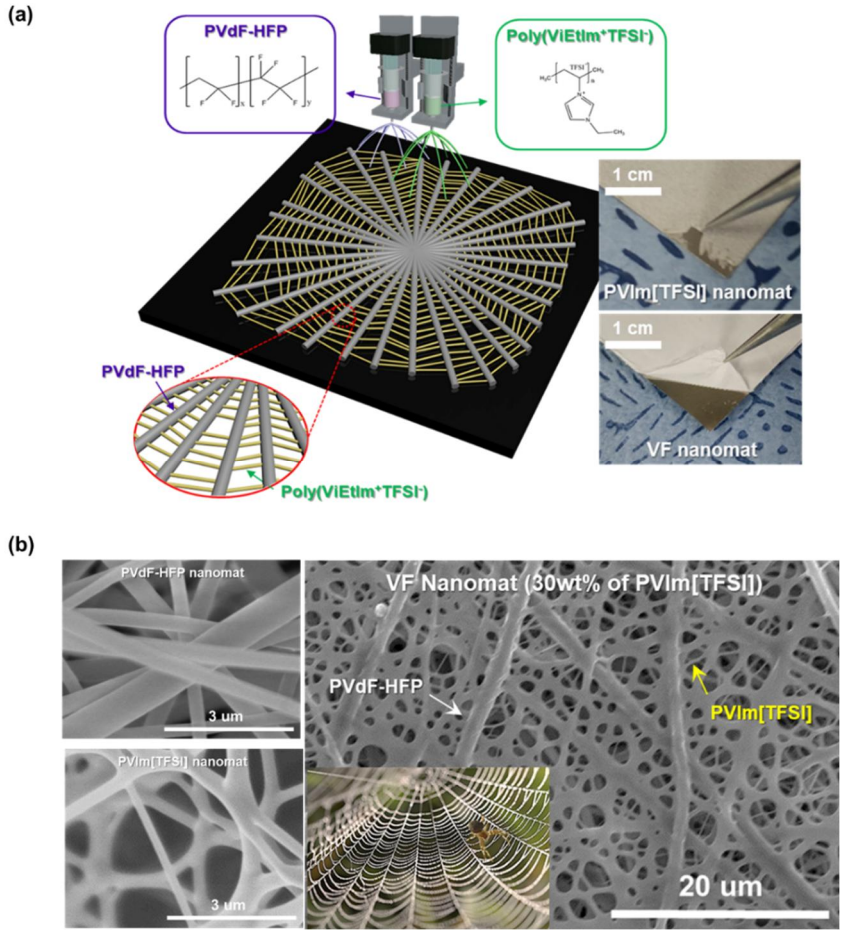

Fig. 12 (a) Schematic illustration depicting dual electrospinning-assisted fabrication of the VF nanomat. Insets are photographs of the VF and PIL nanomats. (b) Morphology of the VF nanomat with spiderweb-like, well-developed porous structure.

3.2.3 Fabrication of spiderweb separator

The electroconductive PEI/MWNT nanomat was inserted between the VF nanomat layer and the PE separator. It can capture the long-chain polysulfides released from the VF-PE separator, as a type of carbonaceous interlayer. PEI nanofibers are conformally wrapped by the MWNTs (yielding a well-developed porous structure (Figure 13a)). This morphological uniqueness is derived from strong intermolecular π- π stacking interaction (between the aromatic rings of PEI and the MWNTs). The PEI/MWNT nanomat shows higher adsorption of polysulfides (Figure 13b). It indicates its potential capability as polysulfide blocking layer. Here, the PEI/MWNT nanomat (3μm) was fabricated directly on PE separator through dual electrospinning (for PEI) and electrospraying (for MWNT). On top of the PEI/MWNT nanomat, the VF nanomat was fabricated as previously described. It resulted in VF nanomat-PEI/MWNT nanomat-PE separator (denoted as VF-IC-PE separator).

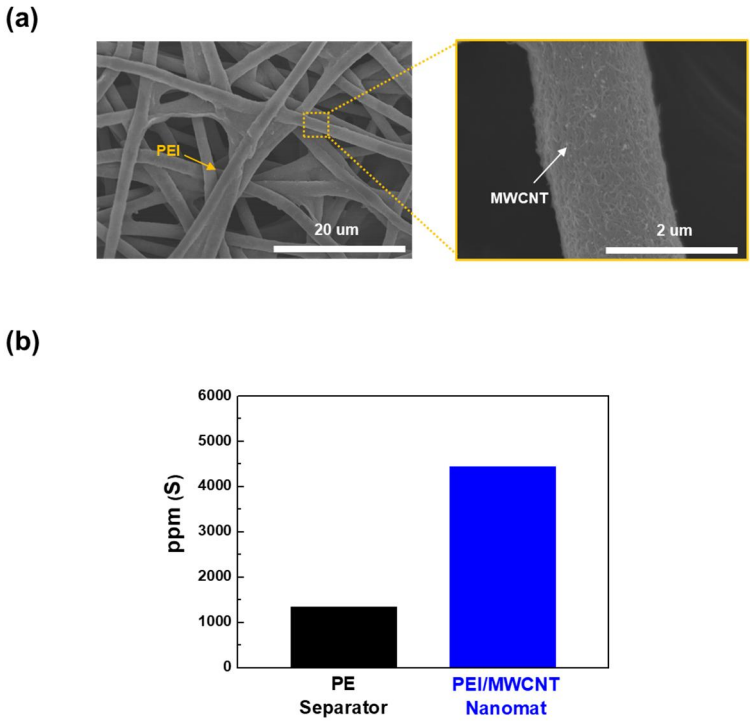

Fig. 13 (a) SEM image at low magnification (left) and high magnification (right). (b) Amount of polysulfides (measured using the ICP analysis) trapped. Prior to this measurement, the separators were soaked in a model polysulfide solution.

3.3 Results and Discussion

3.3.1 Characterizations of PIL for anion-exchange mechanism

The synthesized PIL was dipped into a model polysulfide solution [35,42] for 24 h. And the amount of trapped polysulfides on the PIL was quantitatively estimated using ICP-MS analysis. Al_2O_3 powders (average particle size = 500 nm) [38,43] were chosen as polysulfide-capturing control sample. The PIL showed the larger amount of polysulfides than Al_2O_3 powder (Figure 14). We admitted that this was a relative comparison, when considering the chelation through Al_2O_3 powders derived from the surface area.

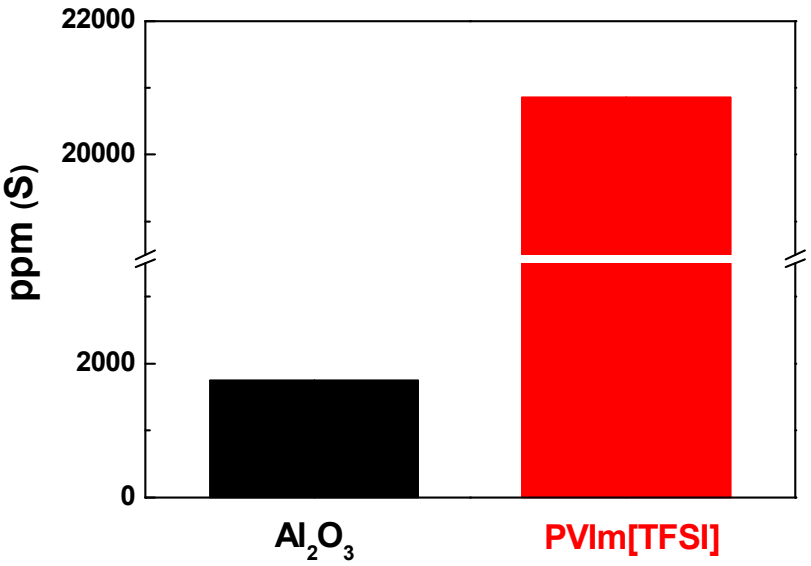

Fig. 14 Amount of polysulfides (measured using the ICP analysis) trapped by: PIL vs. Al_2O_3. First, the PIL and Al_2O_3 were dipped into a polysulfides solution (5 mM Li_2S_6 in DOL/DME = 1/1 (v/v)) for 24 h.

As additional evidence for polysulfide-capturing capability of PIL, UV-vis spectra of the polysulfide solutions was explored depending on polysulfides concentration (Figure 15a). The intensity of peak around 280 nm, related with S_6^{2-} and S_8^{2-} specie,[44-46] was weakened with increase of PIL concentration. It showed the decrease in polysulfide content of solution. In addition to capturing ability of polysulfides explained above, the releasing polysulfides capability of PIL was estimated. The PIL trapping polysulfides was rinsed for removing residual polysulfides on PIL surface. Then, the resultant PIL was immersed into electrolyte solution without polysulfides. Then, we observed the change through the UV-vis spectra result of the electrolyte. The electrolyte solution including PIL with trapping polysulfides exhibited a absorption peak at 280 nm[44-46]. However, the pristine electrolyte solution (Figure 15b) showed the releasing polysulfide from PIL. The above results explained that the PIL conducted diffusion-driven anion-exchange mechanism of polysulfides. The reversible capturing/releasing of polysulfides can be expected for cycling in Li-S batteries.

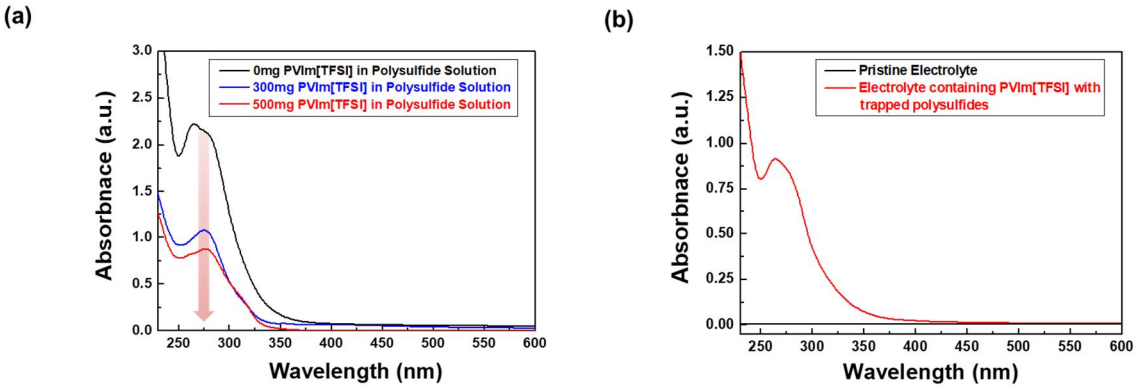

Fig. 15 (a) UV-Vis spectra of polysulfides (Li_2S_6) solution depending on PIL concentration. (b) UV-Vis spectra: pristine electrolyte solution (1 M LiTFSI in DOL/DME = 1/1 (v/v), without poysulfides) vs. electrolyte solution containing the PIL with the trapped polysulfides.

3.3.2 Characterizations of VF nanomat for anion-exchange mechanism

The unusual polysulfide-capturing/-releasing capability of the spiderweb-mimic, PVIm[TFSI]/PVdF-HFP nanomat (denoted as "VF nanomat") was investigated by conducting similar experiments. To verify that this advantageous effect can be attributed to PVIm[TFSI], a supplementary experiment was conducted.

PVIm[TFSI] and PVdF-HFP were dipped into the polysulfide solution and the color change of the solution was examined after 24 h. For polymer contents of 300 and 500 mg, the dark yellow solution became transparent with the PVIm[TFSI], whereas no significant color change was observed with the PVdF-HFP (Figure 16a). The VF nanomat was dipped into the model polysulfide solution (5 mM Li_2S_6 in DOL/DME = 1/1 (v/v)) for 24 h, and the amount of polysulfides trapped by the VF nanomat was estimated using an ICP-MS analysis. The VF nanomat showed a superior polysulfide-capturing capability compared to that of a PE separator used as a control sample (Figure 16b). Meanwhile, to elucidate that the $TFSI^-$ anions of the PVIm[TFSI] in the VF nanomat undergo an anion exchange reaction with the polysulfides, the variation in the nitrogen content of the polysulfide solution containing the VF nanomat (or PE separator) was traced as a function of time using an elemental analyzer (EA) technique (Figure 16c). For the VF nanomat, the nitrogen content in the solution showed a tendency to increase with the elapsed time. In comparison, the PE separator showed no change in the nitrogen content. This result confirms the anion exchange reaction of the $TFSI^-$ anions (originating from the PVIm[TFSI] of the VF nanomat) with the polysulfides.

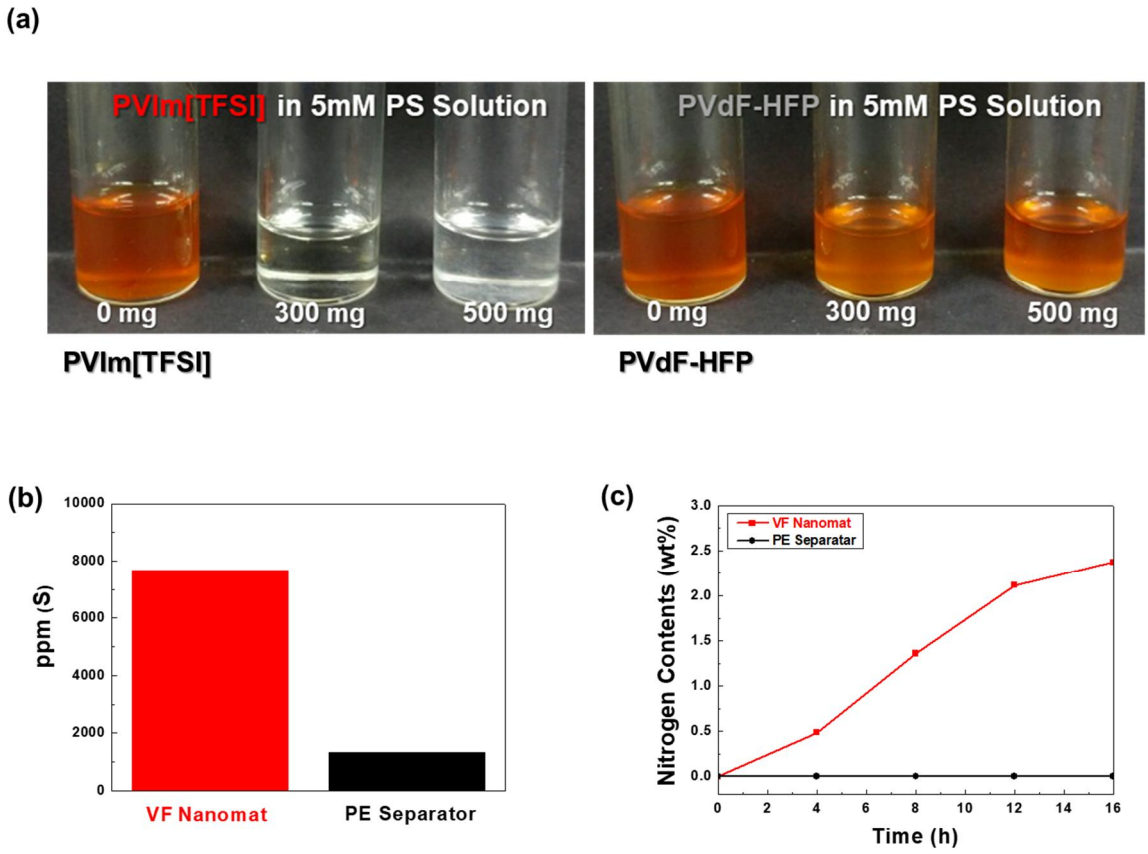

Fig. 16 (a) Photographs showing color change of polysulfides (Li_2S_6) solution as a function of PIL and PVdF-HFP concentration. PIL and PVdF-HFP were respectively dipped into the polysulfide solutions and the color change of the solutions was monitored after 24 h. (b) Amount of polysulfides (measured using the ICP analysis) trapped by: VF nanomat vs. PE separator. (c) Variation of nitrogen content in the polysulfide solution containing the VF nanomat (or PE separator) as a function of time.

The VF nanomat (thickness = 6 μm) was deposited on a commercial PE separator (thickness = 20 μm) using a dual electrospinning process to yield a bilayered, VF nanomat (as the active layer)-PE separator (as the support layer) (hereinafter, referred to as the VF-PE separator). A coin Li-S cell (sulfur cathode/Li metal anode, 1 M LiTFSI in DOL/DME = 1/1 (v/v) with 2 wt% $LiNO_3$ additive) was assembled with the VF-PE separator. The Li-S cell was discharged to 2.15 and 1.50 V. Then, the separator obtained at the two voltages and its structural change was investigated. The VF-PE separator taken at 2.15 V presented a higher sulfur content than the one taken at 1.50 V (Figure 17a). During the discharge reaction (e.g., at 2.15 V), a considerable amount of soluble long-chain polysulfides, which dissolved from the sulfur cathode, exists in the bulk liquid electrolyte. It is thought that the soluble long-chain polysulfides are trapped by the VF-PE separator through an anion exchange reaction with the $TFSI^-$ anions of the PVIm[TFSI]. Meanwhile, after the full discharge (i.e., 1.50 V), the concentration of the long-chain polysulfides in the bulk liquid electrolyte may decrease due to the chelation by the VF-PE separator and the electrochemical transformation[5,14,36,37] of long-chain polysulfides to insoluble low-order Li_2S_2/Li_2S. Under this condition, concentration gradient of the long-chain polysulfides is established between the VF-PE separator and bulk liquid electrolyte. As a consequence, the long-chain polysulfides trapped by the VF-PE separator can be released into the bulk liquid electrolyte to reach concentration equilibrium.

The Li-S cells assembled with the VF-PE and PE separators were cycled at a charge/discharge current density of 0.5 C/0.5 C (Figure 17b), and the electrolyte without $LiNO_3$ (which is well known as a shuttle effect-suppressing additive) was used to clarify the separator contribution. As expected, the cells with the PE separator showed a serious shuttle effect (indicated by the low initial coulombic efficiency (~ 27 %)). In comparison, a significant improvement in the initial coulombic efficiency (~ 72 %) was observed with the VF-PE separator. However, the obtained coulombic efficiency value was not high enough to ensure a reliable cycling performance. Note that the long-chain polysulfides released from the VF-PE separator (after the full discharge) could migrate toward the Li metal anode as well as the sulfur cathode, which may cause an unwanted shuttle effect and the deposition of insoluble low-order polysulfides.

This discharge voltage-dependent, trap/release of the long-chain polysulfides by the VF-PE separator was further verified by an X-ray photoelectron spectroscopy (XPS) analysis (Figure 17c). The characteristic S 2p peak at approximately 163 eV, which is ascribed to long-chain polysulfides,[47-53] was clearly observed at 2.15 V. In comparison, the peak was considerably weaker at 1.50 V. These ICP-MS and XPS results confirmed that the soluble long-chain polysulfides are reversibly captured and released by the VF-PE separator via an anion exchange reaction with the $TFSI^-$ anions of the PVIm[TFSI] as a

function of DOD.

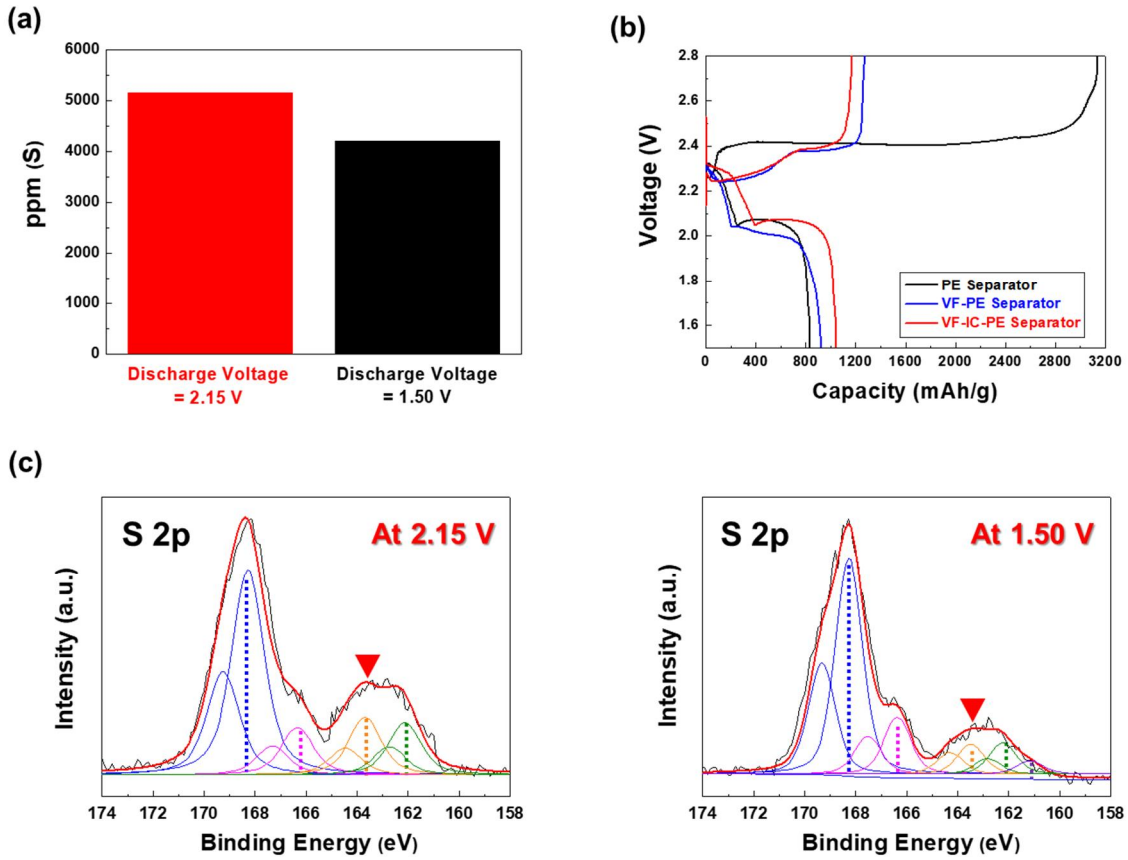

Fig. 17 (a) Amount of polysulfides (measured using the ICP analysis) trapped in VF-PE separator : at different discharge voltages of 2.15 and 1.50 V. (b) Charge/discharge profiles (1st cycle) of the Li-S cells: assembled with the PE, VF-PE and VF-IC-PE separators. The sulfur cathode, Li metal anode and liquid electrolyte were used. The cells were charged/discharged at 0.5 C/0.5 C. (c) XPS S 2p spectra of VF-PE separator: 2.15 and 1.50 V.

3.3.3 Basic membrane properties of spiderweb separator

In Li-S batteries, the so-called upper current collectors[20-26] are known to promote utilization of sulfur active materials and facilitate redox reaction kinetics. Herein, another PEI/MWCNT nanomat was also introduced on top of the VF-IC-PE separator as an electron/ion-conductive upper current collector. Unfortunately, a direct fabrication of the PEI/MWCNT nanomat onto the VF-IC-PE separator was not successful, because the PVIm[TFSI] of the VF nanomat was structurally disrupted upon exposure to the solvent mixture of water/IPA used for the MWCNT suspension. To resolve this problem, the PEI/MWCNT nanomat was independently fabricated through concurrent electrospinning/electrospraying and then laminated with the as-prepared VF-IC-PE separator using a roll-pressing method at room temperature, resulting in the multilayered IC-VF-IC-PE separator (hereinafter, referred to as a "spiderweb separator"). The stepwise fabrication procedure of the spiderweb separator is conceptually shown in Figure 18a along with its photographs.

Due to the asymmetric architecture, different colors were observed on the top (black color from the top layer of the PEI/MWCNT nanomat) and bottom (white color from the PE separator) sides. The roles of the three sandwich-type, functional nanomats (*i.e.*, top (3 μm) and bottom (3 μm) layers = PEI/MWCNT nanomats, middle layer (6 μm) = PVIm[TFSI]/PVdF-HFP nanomat) in the spiderweb separator are schematically illustrated in Figure 18a, along with their multilayered, porous structures (Figure 18b).

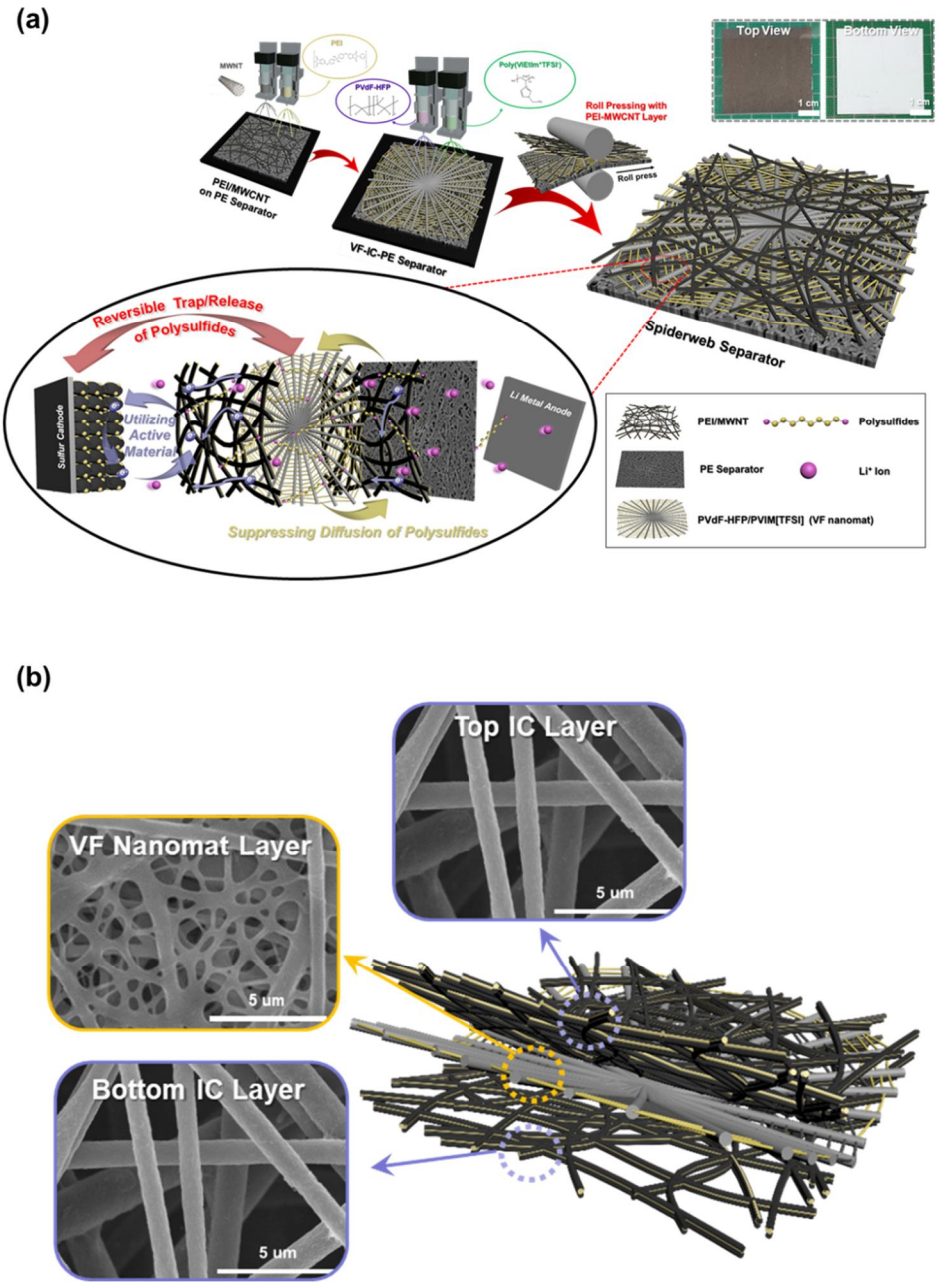

Fig. 18 Fabrication of spiderweb separators and their application to Li-S batteries. (a) Schematic illustration depicting the stepwise fabrication process (bottom nanomat (PEI/MWCNT) → middle nanomat (PIL/PVdF-HFP) → top nanomat (PEI/MWCNT)) of the spiderweb separator, along with its photographs. The nanomats were fabricated through two nozzle-based dual electrospinning (or concurrent electrospinning/electrospraying) processes. (b) SEM images showing the surface of each layer of the spiderweb separator.

Prior to applying the spiderweb separator to Li-S cells, its basic membrane characteristics were investigated. As described previously, all layers of the spiderweb separator have a well-developed porous morphology, which contributes to its high ionic conductivity (= 1.17 mS cm^{-1}) after being filled with liquid electrolytes (Figure 19a). The structural stability of the spiderweb separator was examined. Neither structural disruption nor detachment of any components was observed after the tape test and crumpling/uncrumpling deformation (Figure 19b). The spiderweb separator trapped a larger amount of polysulfides than the PE separator (Figure 19c). This superior polysulfide-capturing capability of the spiderweb separator was further verified by monitoring the variation of the open circuit voltage (OCV) of the cells as a function of elapsed time (Figure 19d).

The OCV of Li-S cells tends to decrease because of the shuttle effect-induced self-discharge problem.[54] The cell with the PE separator showed a sharp decay in the OCV after 75 h, compared with the spiderweb separator presented a higher value of approximately 2.38 V and remained almost unchanged for 150 h. This result demonstrates that the spiderweb separator effectively resolved the self-discharge problem of Li-S cells possibly due to its excellent polysulfide-capturing capability.

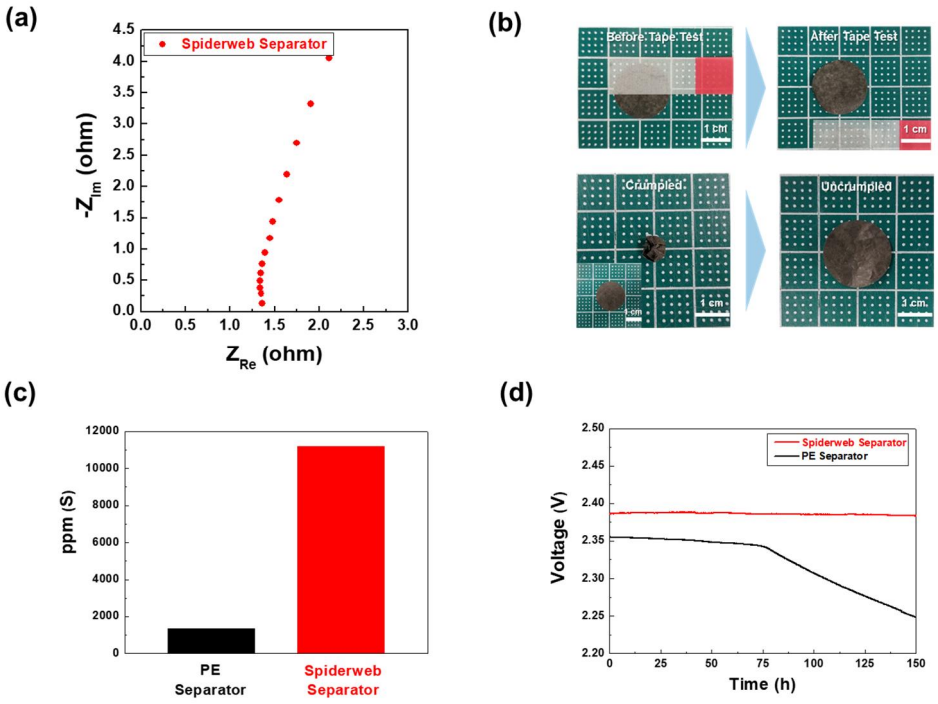

Fig. 19 Basic membrane characteristics of the spiderweb separator. (a) Nyquist plot of the spiderweb separator filled with liquid electrolyte. (b) Mechanical flexibility tests (tape test and crumpling deformation). (c) Amount of polysulfides trapped by the separators and (d) OCV profiles of the Li-S cells as a function of elapsed time (vs. PE separator).

3.3.4 Electrochemical performance of spiderweb separator

The charge/discharge performance of Li-S cells assembled with the spiderweb separator (and the PE separator as a control sample) was investigated, in which a sulfur cathode (sulfur active materials/carbon black conductive additive/SBR-CMC binder = 75/20/5 (w/w/w)), Li metal anode and liquid electrolyte (1 M LiTFSI in DOL/DME = 1/1 (v/v) with 2 wt% $LiNO_3$ additive) were used. The cells were cycled between 1.7 and 2.8 V at a charge/discharge current density of 2.0 C/2.0 C. Two typical charge/discharge plateaus[55] were observed for the cells. The spiderweb separator showed higher initial charge/discharge capacities and longer discharge plateaus than the PE separator (Figure 20a). In addition, the cell containing the spiderweb separator provided a substantial improvement in the cycling performance (capacity retention after 300 cycles = 72 % vs. 23 % for the PE separator) (Figure 20b).

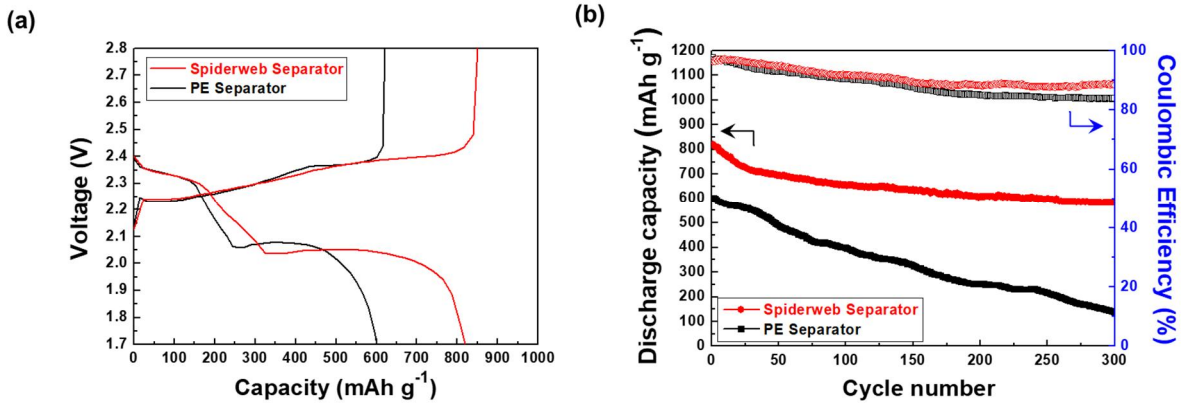

Fig. 20 (a) Initial charge/discharging profiles of Li-S cells with the spiderweb and PE separators. The sulfur cathode, Li metal anode and liquid electrolyte were used. The cells were cycled at 2.0 C/2.0 C. (b) Cycling performance (charge/discharge current density = 2.0 C/2.0 C) of the Li-S cells assembled with the spiderweb and PE separators.

This excellent cell performance of the spiderweb separator was also observed at the high areal sulfur loading (areal sulfur loading = 4.5 mg cm^{-2}) (Figure 21a). Note that the porous structure of the spiderweb separator was maintained after the cycling test (Figure 21b), revealing robust structural stability. These results underscored the combined effect (specifically, the suppression of the shuttle effect and the better utilization/facilitation of the redox reaction kinetics of sulfur active materials) of the sandwich-type functional nanomats in the spiderweb separator on the charge/discharge performance of the Li-S cells.

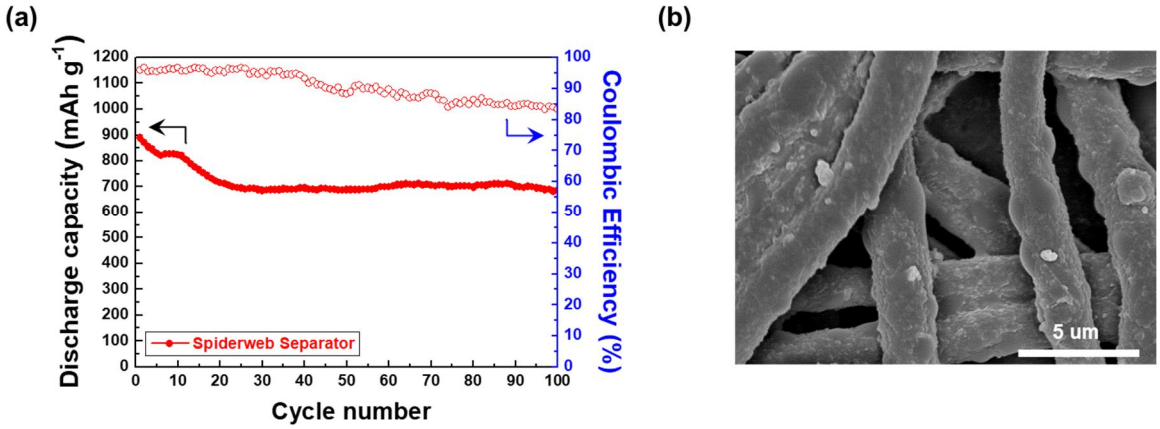

Fig. 21 (a) Cycle performance (charge/discharge current density = 0.5 C/0.5 C) (areal sulfur loading = 4.5 mg cm^{-2}) assembled with the spiderweb separator. (b) SEM images of the spiderweb separator after 200 charge/discharge cycles at top nanomat (PEI/MWCNT) adjacent to the sulfur cathode.

This advantageous role of the spiderweb separator was confirmed by measuring the change in the charge transfer resistance (R_{CT}) of the cells as a function of DOD (Figure 22). As the discharge reaction proceeded, the R_{CT} of the cells showed a tendency to increase and became pronounced at the fully discharge state, indicating the unwanted generation of insoluble low-order polysulfides and their deposition onto the electrodes.[56,57] In contrast, the growth of the R_{CT} was remarkably suppressed at the spiderweb separator, which demonstrated its beneficial contribution to preventing the shuttle effect.

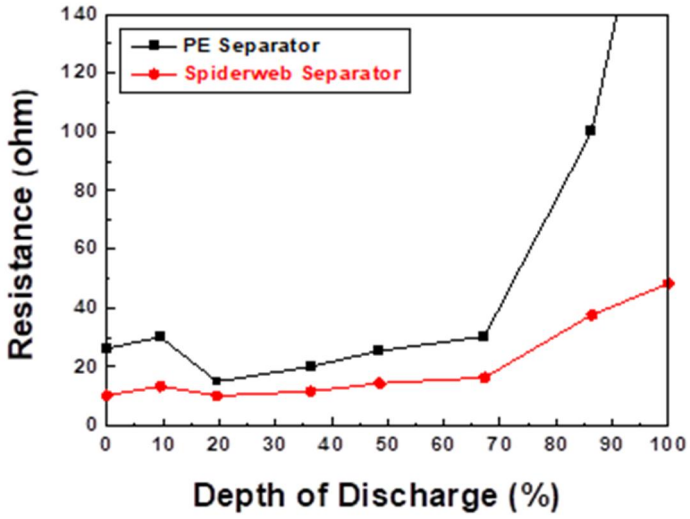

Fig. 22 Changes in charge transfer resistance (R_{CT}) of the Li-S cells: with the spiderweb and PE

separators depending on depth of discharge (DOD).

A post-mortem analysis of the cycled Li-S cells was conducted to further elucidate the effects of the spiderweb separator. After the cycling test (200 cycles at 2.0 C/2.0 C), the cells were disassembled, and their major components including the sulfur cathodes, Li metal anodes and separators were analyzed. Figure 23a shows that the sulfur cathode assembled with the spiderweb separator maintained its porous structure without a structural change/disruption. In comparison, for the cell containing the PE separator (inset of Figure 23a), the cathode surface was seriously contaminated and even blocked by unwanted resistive layers[58-60] that are believed to be electrochemically inactive sulfur species. The surface of the Li metal anode after the cycling test was investigated by measuring the amount of deposited polysulfides. Figure 23b shows that a substantially lower sulfur content was detected on the Li metal anode assembled with the spiderweb separator compared to that with the PE separator, verifying that the spiderweb separator effectively suppressed the migration of the polysulfides toward the Li metal anode. To better understand the separator-dependent structural change of the electrodes described above, the surface of the separators facing the Li metal anodes was examined using an XPS analysis (Figure 23c). The characteristic peaks in the range of 160-166 eV, which correspond to Li_2S_x,[47-52] were considerably weaker with the spiderweb separator than the PE separator. Moreover, particular attention was paid to the characteristic peak at 167.0 eV, which is ascribed to electrically insulating/electrochemically irreversible lithium sulfate (Li_xSO_y) compounds that exert harmful influence on the charge/discharge reaction of Li-S cells.[61-63] Note that the spiderweb separator showed a remarkably weaker peak intensity at 167.0 eV than the PE separator, confirming its beneficial effect on the suppression of polysulfide migration toward the Li metal anodes.

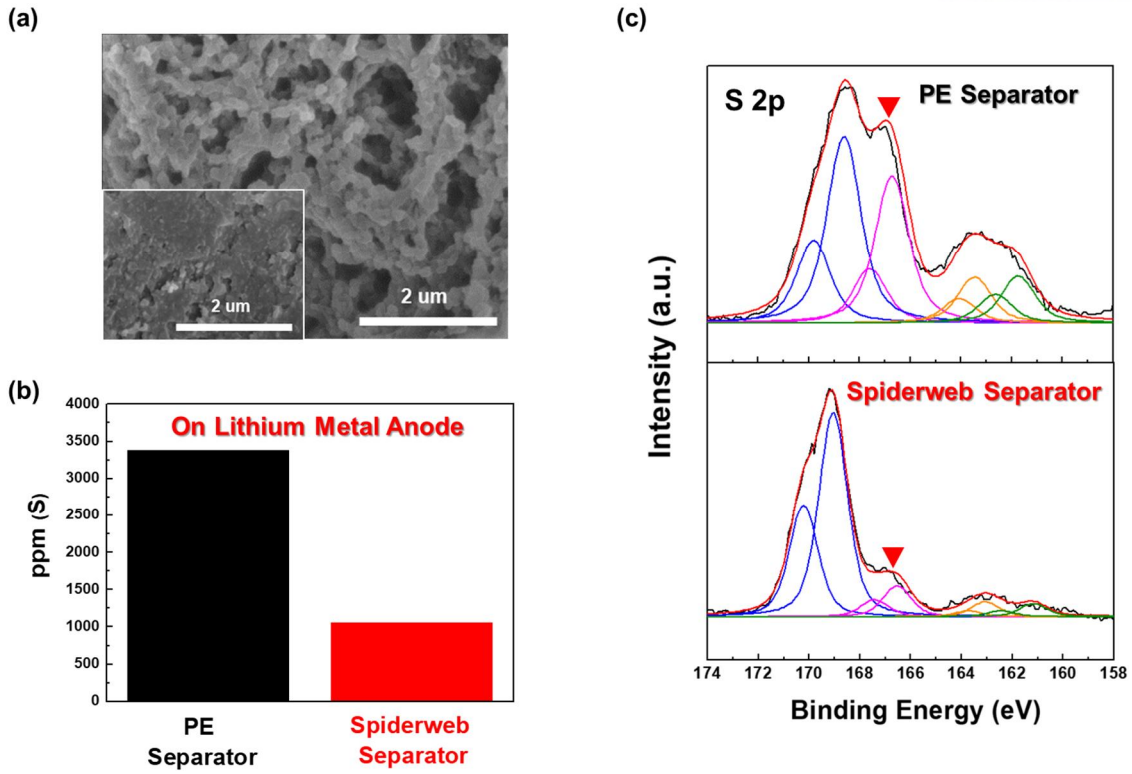

Fig. 23 Post-mortem analysis (after 200 cycles) of cells. (a) SEM image of the sulfur cathodes. (b) Polysulfides amount deposited on the lithium metal anodes. (c) XPS S 2p spectra of separator adjacent to the lithium metal anodes.

3.4 Conclusion

In summary, we described spiderweb-mimic, anion-exchangeable separators based on polyionic liquids (here, PVIm[TFSI]) as a membrane-driven strategy for the development of high-performance Li-S batteries. The spiderweb separator consisted of sandwich-type, three functional nanomats (top and bottom layers = PEI/MWCNT nanomats, middle layer = PVIm[TFSI]/PVdF-HFP nanomat) on top of a PE separator. These three nanomats were fabricated through dual electrospinning (for the middle nanomat) and concurrent electrospinning/electrospraying (for the top and bottom nanomats) processes. The middle nanomat, in which the PVIm[TFSI] nanofibers were highly reticulated between the PVdF-HFP nanofibers, played a vital role in the discharge voltage-dependent, reversible trap/release of polysulfides via the anion exchange reaction between their $TFSI^-$ anions and the polysulfides. Meanwhile, the PEI/MWCNT nanomats act as an upper current collector (top nanomat: adjacent to the sulfur cathodes) to boost the electrochemical redox reaction of the sulfur cathodes and as a blocking layer (bottom nanomat: facing the PE separator) to suppress the crossover of polysulfides to the Li metal anode. Benefiting from the unique nanomat structure and chemical functionalities that have never been reported in Li-S battery separators, the spiderweb separator effectively prevented the shuttle effect while ensuring facile Li ion transport between the electrodes, leading to exceptional improvement in the cell performance (capacity (at a current density of 2.0 C) = 819 mAh g^{-1} and cycling retention (at 2.0 C/2.0 C) = 72 % after 300 cycles) that lies far beyond those achievable with conventional Li-S battery technologies. We envision that the spiderweb separator presented herein holds great promise as a versatile and effective membrane platform technology for potential use in a variety of advanced power sources and permselective separation applications.

3.5 References

1. Y. Cui et al., *Chem. Soc. Rev.* **2013**, *42*, 3018.
2. A. Manthiram et al., *Adv. Energy Mater.* **2016**, *6*, 1501480.
3. A. Manthiram, et al., *Acc. Chem. Res.* **2013**, *46*, 1135.
4. J. M. Tarascon et al., *Nat. Mater* **2011**, *11*, 19.
5. A. Manthiram et al., *Adv. Funct. Mater.* **2014**, *24*, 5299.
6. B. Wei et al., *Nano Energy*. **2015**, *15*, 413.
7. Z. Sun et al., *Nat. Commun.* **2017**, *8*, 14627.
8. J. Liang et al., Cheng, *Energy Storage Materials.* **2016**, *2*, 76.
9. L. F. Nazar et al., *J. Mater. Chem.* **2010**, *20*, 9821.
10. A. Manthiram et al., *Adv. Mater.* **2015**, *27*, 1980.
11. L. Ji et al., *J. Am. Chem. Soc*. **2011**, *133*, 18522.
12. J. -Q. Huang et al., *Energy Environ. Sci.* **2014**, *7*, 347.
13. A. Manthiram et al., *Acc. Chem. Res*. **2013**, *46*, 1125.
14. A. Manthiram et al., *Chem. Rev.* **2014**, *114*, 11751.
15. S. Yuan et al., *Adv. Energy Mater.* **2016**, *6*, 1501733.
16. L. F. Nazar et al., *Adv. Mater.* **2015**, *27*, 6021.
17. Z. Li et al., *Angew. Chem. Int. Ed.* **2015,** *54*, 12886.
18. Y. Xiang et al., *ChemSusChem.* **2016**, *9*, 3023.
19. A. Manthiram et al., *Chem. Commun.* **2012**, *48*, 8817.
20. G. Zhou et al., Cheng, *Adv. Mater.* **2015**, *27*, 641.
21. S. H. Chung et al., *Chem. Commun.* **2014**, *50*, 4184.
22. A. Manthiram et al., *Nat. Commun.* **2012**, *3*, 1166.
23. C. Zu et al., *Phys. Chem. Chem. Phys.* **2013**, *15*, 2291.
24. Y. Cui et al., *Energy Environ. Sci.* **2014**, *7*, 3381.
25. X. Wang et al., *J. Power Sources.* **2013**, *242*, 65.
26. Q. Zhang et al., *Adv. Energy Mater.* **2017**, *7*, 1700260.
27. G. Wang et al., *Small Methods.* **2017**, *1*, 1700089.
28. F. Wei et al., *Energy Storage Materials.* **2015**, *1*, 127
29. Q. Zhang et al., *Small.* **2016**, *12*, 381.
30. Z. Bakenov et al., *J. Energy Chem.* **2017**, *26*, 1276.
31. X. Wu et al., *J. Power Sources.* **2015**, *273*, 511.
32. J. H. Kim et al., *ACS Appl. Mater. Interfaces.* **2016**, *8*, 20092.
33. X. Liu et al., *J. Power Sources.* **2012**, *218*, 163.
34. S. Kaskel et al., *J. Power Sources.* **2014**, *251*, 417.
35. Y. Cui et al., *Nat. Commun.* **2016**, *7*, 11203.

36. S. Evers, T. Yim, L. F. Nazar, *J. Phys. Chem. C.* **2012**, *116*, 19653.
37. L. F. Nazar et al., *Nat. Commun.* **2011**, *2*, 325.
38. S. Y. Lee et al., *Nano Lett.* **2017**, *17*, 2220.
39. F. Yan et al., *J. Mater. Chem.* **2012**, *22*, 18018.
40. Zou, *J* et al., *Mater. Chem. A.* **2014**, *2*, 20147.
41. J. -H. Wang et al., *RSC. Adv.* **2014**, *4*, 61936.
42. G. Shao et al., *J. Power Sources.* **2017**, *348*, 175
43. J. Li et al., *Electrochim. Acta.* **2014**, *129*, 55.
44. Z. Wen et al., *Phys. Chem. Chem. Phys.* **2016**, *18*, 29293.
45. H. H. Kung et al., *ChemSusChem.* **2014**, *7*, 2545.
46. S. Huang et al., *Adv. Mater.* **2015**, *27*, 2891.
47. A. Manthiram et al., *Nat. Commun.* **2013**, *4*, 2985.
48. S.-Y. Lee et al., *Nano Lett.* **2016**, *16*, 3292.
49. A. Manthiram et al., *Angew. Chem.* **2013**, *125*, 7068.
50. A. Manthiram et al., *Adv. Energy Mater.* **2014**, *4*, 1400897.
51. X. Hong et al., *J. Electrochem. Soc.* **2012**, *159*, 1816.
52. L. F. Nazar et al., *Nat. Commun.* **2013**, *6*, 5682.
53. S.-Y. Lee et al., *Adv. Funct. Mater.* **2016**, *26*, 7074.
54. D. Wang et al., *ACS. Appl. Mater. Interfaces.* **2014**, *6*, 8006.
55. K. Xu et al., *Chem. Rev.* **2014**, *114*, 11503.
56. Y. Kim et al., *Phys. Chem. Chem. Phys.* **2012**, *14*, 6796.
57. Y. Liu et al., *J. Electrochem. Soc.* **2013**, *160*, 553.
58. Y. Cui et al., *Energy Environ. Sci.* **2014**, *7*, 3381.
59. Q. Zhang et al., *Adv. Mater.* **2016**, *28*, 9551.
60. K. Amine et al., *ACS. Appl. Mater. Interfaces.* **2014**, *6*, 21938.
61. L. Mai et al., *Adv. Mater.* **2017**, *29*, 1601759.
62. X. W. Lou et al., *Nat. Commun.* **2014**, *5*, 5002.
63. J. -G. Zhang et al., *Adv. Funct. Mater.* **2016**, *26*, 3059.

Chapter IV. Anode-customized Functional Separators for Lithium-Metal Battery

4.1 Introduction

The forthcoming ubiquitous electronics era, which will find widespread use of the Internet of Things, flexible/wearable devices, and electric vehicles, has led to the pursuit of high-energy-density power sources with electrochemical sustainability.[1,2] Among the numerous power sources reported to date, lithium-ion batteries (LIBs) have been widely used in various applications. However, LIBs are still struggling to meet the continuously increasing demand for high-energy-density applications. Li metal electrodes have recently garnered considerable attention as a promising material approach to resolve this issue, because of their low weight, low electrode potential (-3.04 V vs. standard hydrogen electrode), low density (0.534 g cm^{-3}), and high theoretical capacity (3860 mAh g^{-1}).[3-5]

Despite having such enormous potential, Li metal electrodes are still away from practical use due to their interfacial instability with electrolytes, formation of Li dendrites, uncontrolled volume changes, and generation of electrically inactive "dead Li".[6] These challenges have forced the use of thick Li metal electrodes (> 100 μm) with low utilization (< 10 %), resulting in serious losses of cell energy density.[7,8]

Various approaches have been implemented to resolve the aforementioned problems of Li metal electrodes, including the synthesis/formulation of new electrolytes,[7-9] the introduction of protective layers (including artificial solid-electrolyte-interphases (SEI) based on organic and inorganic materials),[10-16] the construction of Li hosts,[17, 18] and the structure/surface control of Li metal electrodes and current collectors.[19, 20] It should be noted that most previous studies have relied on petroleum-derived hydrocarbon chemicals, inorganic/metallic substances, and their composites/alloys. These traditional synthetic materials, unfortunately, often fail to fully address the aforementioned formidable challenges facing Li metal electrodes.

Here, we present cholesteric liquid crystalline (cLC) cellulose nanocrystal (CNC) skin for sustainable Li metal electrodes as a natural material strategy. CNCs, which are generally obtained by hydrolysis of renewable and abundant cellulose, are crystalline rod-shaped nanomaterials (5 ~ 30 nm in diameter and 100 ~ 250 nm in length).[21] CNCs have unique characteristics such as nanoscale dimensions, high aspect ratios, high modulus, and easy chemical modification, rendering CNCs useful for various applications.[21, 22] Notably, CNCs can show a peculiar LC behavior[22, 23] that leads to the formation of self-organized phases called as cholesteric (or chiral nematic) LCs. In this study, the cLC-

CNC skin is rationally designed to achieve a precisely defined nanoporous structure with optimal tortuosity. The following benefits can be expected from the cLC-CNC skin: i) skin thickness (1 μm) enables negligible loss in energy densities of resulting Li metal electrodes, ii) high mechanical modulus of the CNCs prevents Li dendrite growth and limits the volume expansion of Li metal electrodes during Li plating/stripping, iii) well-ordered nanoporous structure of the cLCs allows facile/uniform ion flux toward Li metal electrodes, and iv) pitch of the cLC-CNC skin can be tuned to vary its porous structure, thereby finely controlling tortuous paths of dendrite growth without hampering ion transport.

Driven by the elaborately designed structure and unique physicochemical properties described above, the cLC-CNC skin improves the cyclability of Li plating/stripping and suppresses Li dendrite growth and volume expansion of Li metal electrodes at various depth of discharge (DOD) conditions. The cLC-CNC skin is applied onto a thin Li metal electrode (20 μm) which is desirable for high-energy-density full cells. The Li metal full cells (composed of Li metal electrodes with the cLC-CNC skin and high-capacity $LiNi_{0.8}Co_{0.1}Mn_{0.1}O_2$ (NCM811) cathodes) exhibit stable charge/discharge cycling performance while maintaining its volumetric energy density. To the best of our knowledge, this is the first study reporting the cLC-CNC skin as a new concept of ion-conducting protective layers for Li metal electrodes.

4.2 Experimental Section

4.2.1 Fabrication of cLC-CNC@Li

CNC suspensions were purchased from the university of MAINE. The CNC suspension (12.1 wt.%) was diluted to 0.12 wt.% using a water/ethanol (= 90/10 (w/w)) mixture. The diluted CNC suspension was poured onto an O_2-plasma treated polyethylene (PE) separator membrane (acting as a porous substrate**)** and then was allowed to slowly dry for approximately 72 h at 25 °C and 45% relative humidity (R.H.) for evaporation-induced self-assembly (EISA) process, producing a CNC thin layer with cLC structure. Meanwhile, a control CNC film was fabricated through the vacuum-assisted self-assembly (VASA) process: the CNC suspension deposited on the PE separator membrane was subjected to vacuum-assisted drying at 60 °C for 36 h. Subsequently, the obtained cLC-CNC film was transferred to Li metal foil electrodes using a simple roll-pressing process at room temperature. Additionally, the pitch of the cLC-CNC layer was systematically tuned by varying the sonication time of the CNC suspension.

The CNC layers were fabricated by pouring the CNC suspension onto an O_2 plasma-treated PE separator through EISA or VASA processes (Figure 24). The details on the fabrication procedure are described in the experimental section. The sulfate groups of the CNCs, which are a prerequisite for producing the cLC structure, were quantitatively detected by EDS analysis.

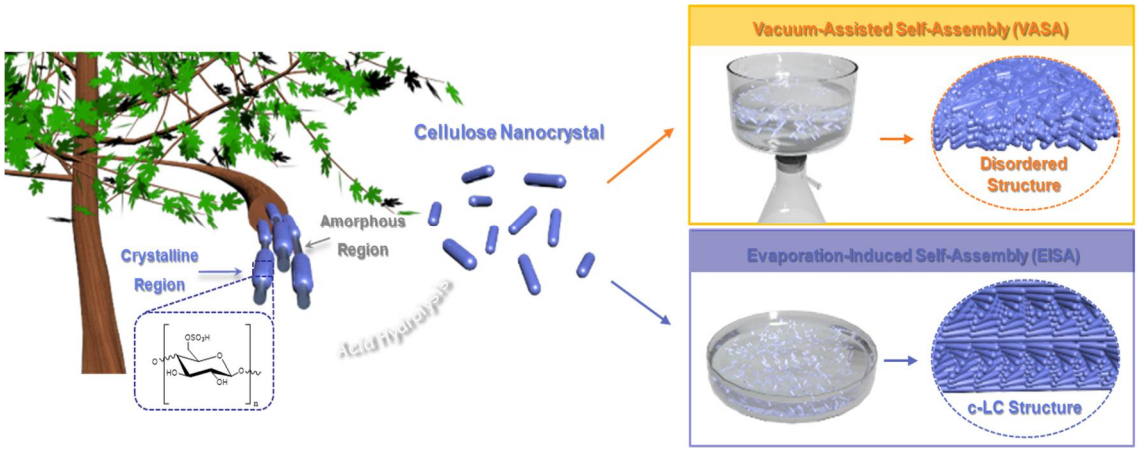

Fig. 24 Schematic illustration depicting the fabrication of CNC layer by vacuum-assisted self-assembly (VASA) and evaporation-induced self-assembly (EISA).

4.2.2 COMSOL simulation of Li-ion flux through the cLC-CNC

The simulation of the Li-ion flux through the CNC layers was conducted using COMSOL Multiphysics software with "Tertiary Current Distribution, Nernst-Planck" physics/2D geometry.[13,16] The overpotential of electrodeposition was set to -200 mV (vs. Li/Li^+) at a working electrode with the relative equilibrium potential of 0 mV, which forms a nonuniform current density distribution in the range of 0.25 - 4.5 mA cm^{-2}. The boundary conditions for the electrolyte adjacent to the electrodes obey the Butler–Volmer equation for electrochemical reaction kinetics. The Li^+ diffusion coefficient (D) of 2.93 x 10^{-6} cm^2 s^{-1} (at 298 K) [13,16] was applied, which was calculated by the Nernst-Einstein relation ($D = \mu RT/zF$) wherein μ is the ionic mobility, R the gas constant, T the absolute temperature, z the ionic charge, and F the Faraday constant.

4.3 Results and Discussion

4.3.1 Characterizations of cLC-CNC skin

The CNC layers produced *via* the EISA technique actively reacted with polarized light (Figure 25a), in contrast to a control CNC sample obtained by the VASA method. The EISA creates highly ordered cLC structure, although it may require longer drying times than the VASA.[24] This characteristic optical behavior of the EISA CNC layers was further investigated by inclined-view cross-sectional SEM analysis (Figure 25b). At an oblique angle to the helical axis of 90°, a continuous wave-like shape, which is a structural feature of cLC, was observed for the EISA CNC layers.[25] It is known that the reflected wavelength of cLC depends on its pitch and refractive index.[26] When half-values of the cLC pitch corresponds to wavelengths of visible light, the resulting cLC appears iridescent. The EISA CNC layers showed a typical iridescent color, whereas the VASA control sample was colorless (Figure 25c). Furthermore, the color of the EISA CNC layers varied with rotation angle (Figure 25d). These results exhibit the successful formation of cholesteric LC structure of CNC layers (cLC-CNC).

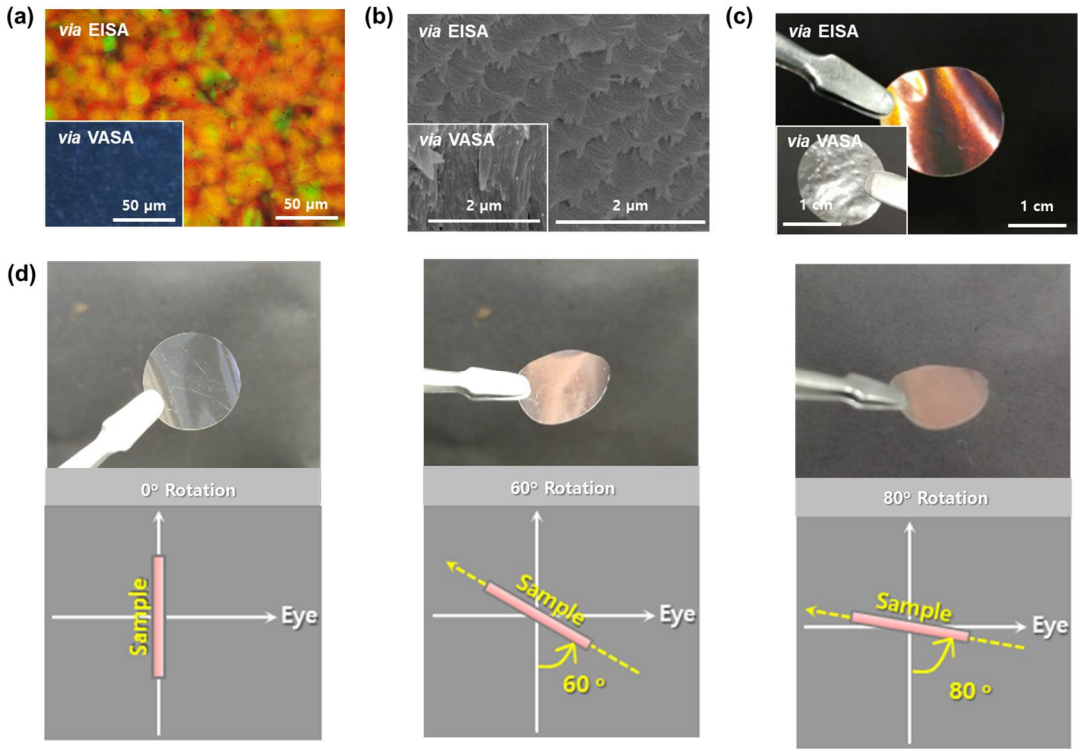

Fig. 25 (a) Polarized optical microscopy images of the CNC layer fabricated via EISA (vs. VASA

(inset)). (b) Inclined-view cross-sectional SEM images of the CNC layer via EISA (vs. VASA (inset)). Photographs of (c) the CNC layer fabricated via EISA (vs. VASA (inset)). (d) different rotation angles.

The cLC-CNC fabricated by the EISA technique was transferred onto a Li metal foil using a simple roll-pressing process[27,28] at room temperature (Figure 26a). The thin cLC-CNC (1 μm in thickness) was deposited on top of the Li metal foil. Neither structural disruption nor detachment of the cLC-CNC was observed after taping tests (Figure 26b), revealing the mechanical stability and good adhesion of cLC-CNC on the Li metal.

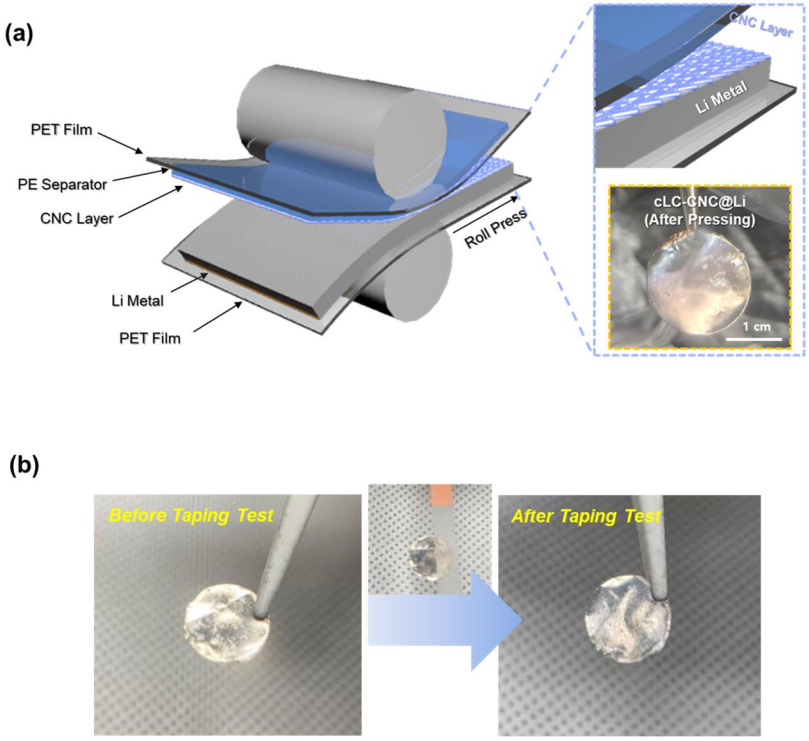

Fig. 26 (a) Schematic illustration depicting the transfer of the cLC-CNC thin film to a Li metal foil using a roll-pressing process at room temperature. (b) Photographs of the cLC-CNC@Li before/after the taping test.

To explore the feasibility of the cLC-CNC as an ion-conducting protective layer for Li metal electrodes, we conducted a Li/Li symmetric cell test, in which Li plating/stripping cycling was performed using a conventional carbonate-based liquid electrolyte (1 M $LiPF_6$ in EC/DEC = 1/1 (v/v) with 10 wt.% FEC and 1 wt.% VC) at a fixed current density of 0.5 mA cm^{-2}. The cLC structure was confirmed by identifying its nanoporous channels (average pore size = 4.5 nm, Figure 27a). Figure 27b shows that the cLC-CNC (fabricated *via* EISA) had stable Li plating/stripping cyclability along with

low polarization, compared to the VASA control sample. This result demonstrates that the cLC-CNC, due to its well-defined cLC structure with the nanoporous channels that are filled with liquid electrolytes), allows uniform and homogeneous ion flux toward the Li metal and prevents random growth of Li dendrites. The facile ion transport through the cLC-CNC was verified by estimating its ionic conductivity (σ = 0.26 mS cm^{-1}, after being soaked with the liquid electrolyte, Fig. 27c).

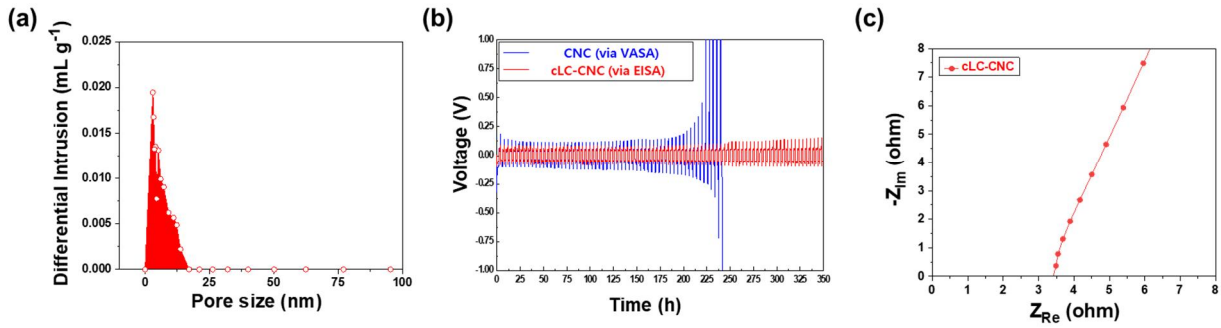

Fig. 27 (a) Schematic illustration depicting the transfer of the cLC-CNC thin film to a Li metal foil using a roll-pressing process at room temperature. (b) Photographs of the cLC-CNC@Li before/after the taping test.

This beneficial effect of the cLC-CNC (fabricated *via* EISA) was theoretically elucidated by simulating its Li-ion flux. A rectangular cell (0.4 μm in height and 0.15 μm in diameter) filled with liquid electrolyte was proposed as a model system for this simulation (Figure 28). A pristine Li metal electrode (Figure 29a), which was chosen as a reference, showed that Li dendrite growth is accelerated by the formation of hot-spots that stem from nonuniform Li nucleation during Li plating and stripping, which was consistent with those of previous works.[13,16,29] For the VASA control sample (Figure 29b), Li ions migrate randomly through the inhomogeneous porous channels with long and tortuous paths. In sharp contrast, the cLC-CNC (fabricated *via* EISA) exhibited the uniform Li-ion flux through the cLC-structured porous channels (Figure 29c). This simulation result is highly consistent with the above-described experimental results of the Li/Li symmetric cell test (shown in Figure 27b).

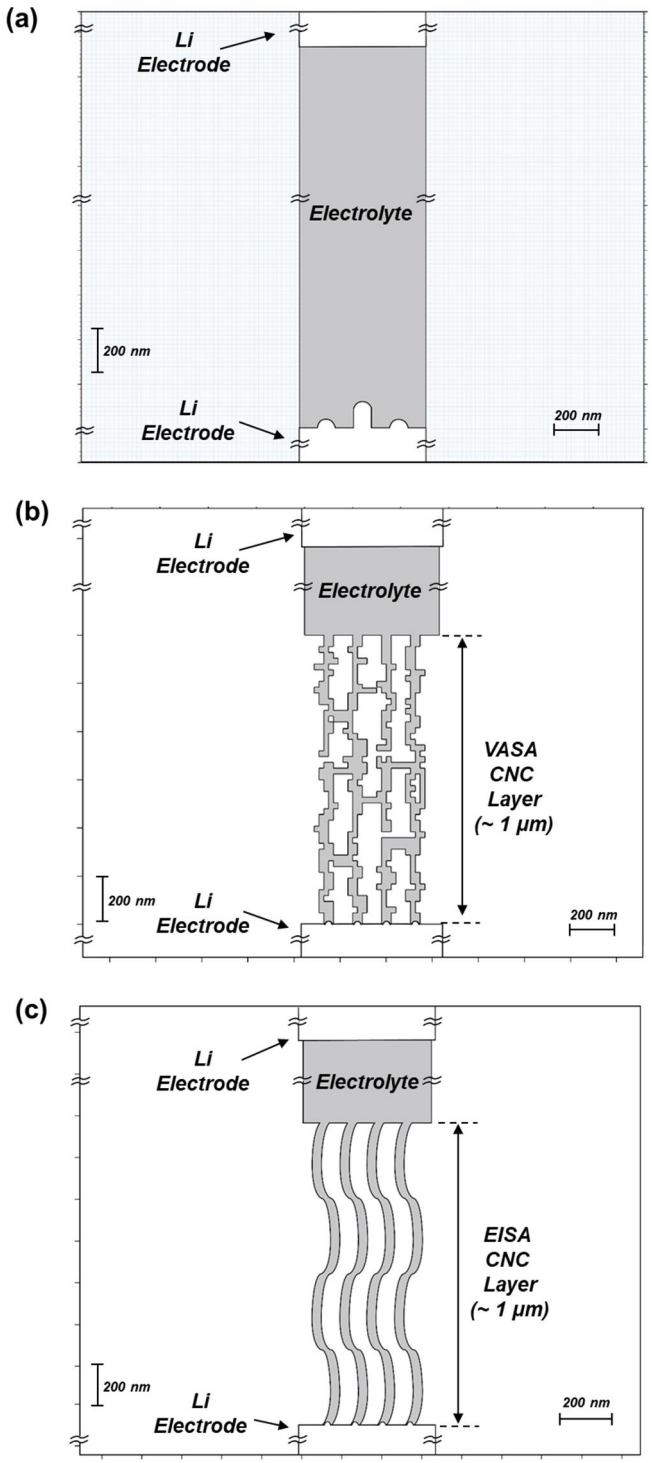

Fig. 28 The COMSOL model domain with boundaries: (a) pristine metal, (b) VASA and (c) EISA CNC film.

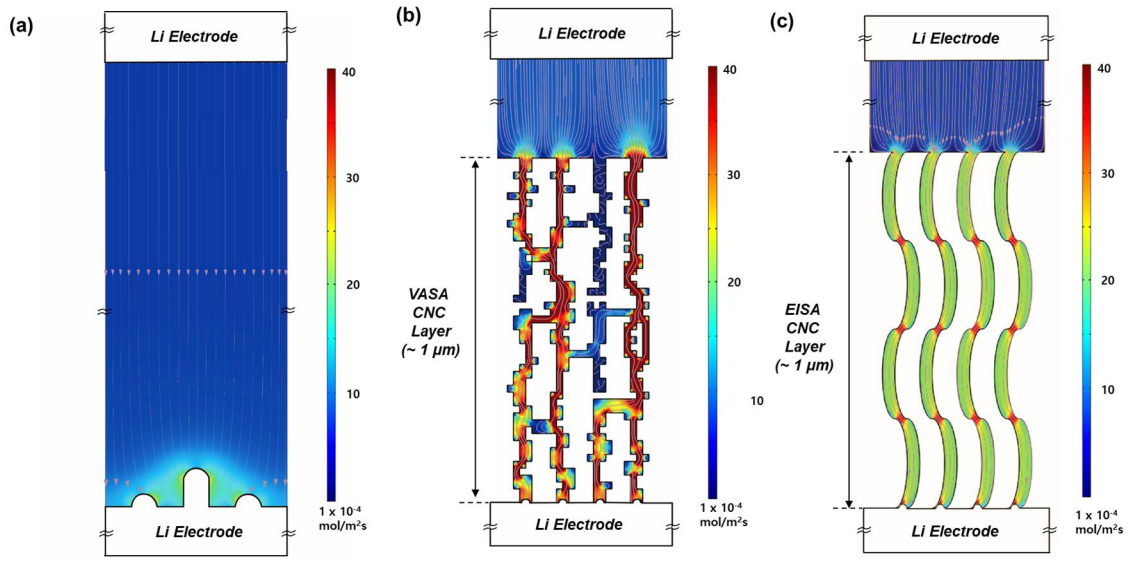

Fig. 29 The COMSOL simulation results of Li-ion flux: (a) pristine metal, (b) VASA and (c) EISA CNC film.

4.3.2 Suppressing Li dendrite growth by cLC-CNC skin

We investigated the effects of the above-prepared cLC-CNC skin on the stabilization of Li metal electrodes. It is known that a high mechanical modulus is required for a protective layer to suppress dendrite propagation.[13,30] The nanoindentation test (Figure 30a) showed that the modulus of the cLC-CNC skin is exceptionally high (> 10 GPa), indicating that it could effectively prevent the growth of Li dendrites (4 GPa[13,31]). To demonstrate this potential benefit of the cLC-CNC skin, a model study was conducted using a Li/Li symmetric cell, in which unidirectional plating current was continuously applied until an internal short-circuit between the two Li metal electrodes occurred (Figure 30b). The pristine Li showed a sharp voltage rise after 72 h, indicating internal short-circuit failure induced by the penetration of Li dendrites. By comparison, no appreciable fluctuation in the voltage profile was observed for the Li metal electrode with the cLC-CNC skin.

Such a noticeable difference between the two samples was further verified by analyzing surface SEM images after the unidirectional plating test (for 72 h). The surface of the Li metal with cLC-CNC skin was smooth and dense with negligible formation of Li dendrites, whereas the pristine Li showed the formation of irregular and filamentary dendrites (Figure 30c). To

better understand the unusual plating behavior of the cLC-CNC skin on Li metal, its cross-sectional morphology was examined (Figure 30d). We note that uniform and dense Li was stably plated underneath the cLC-CNC skin without noticeable dendrite growth.

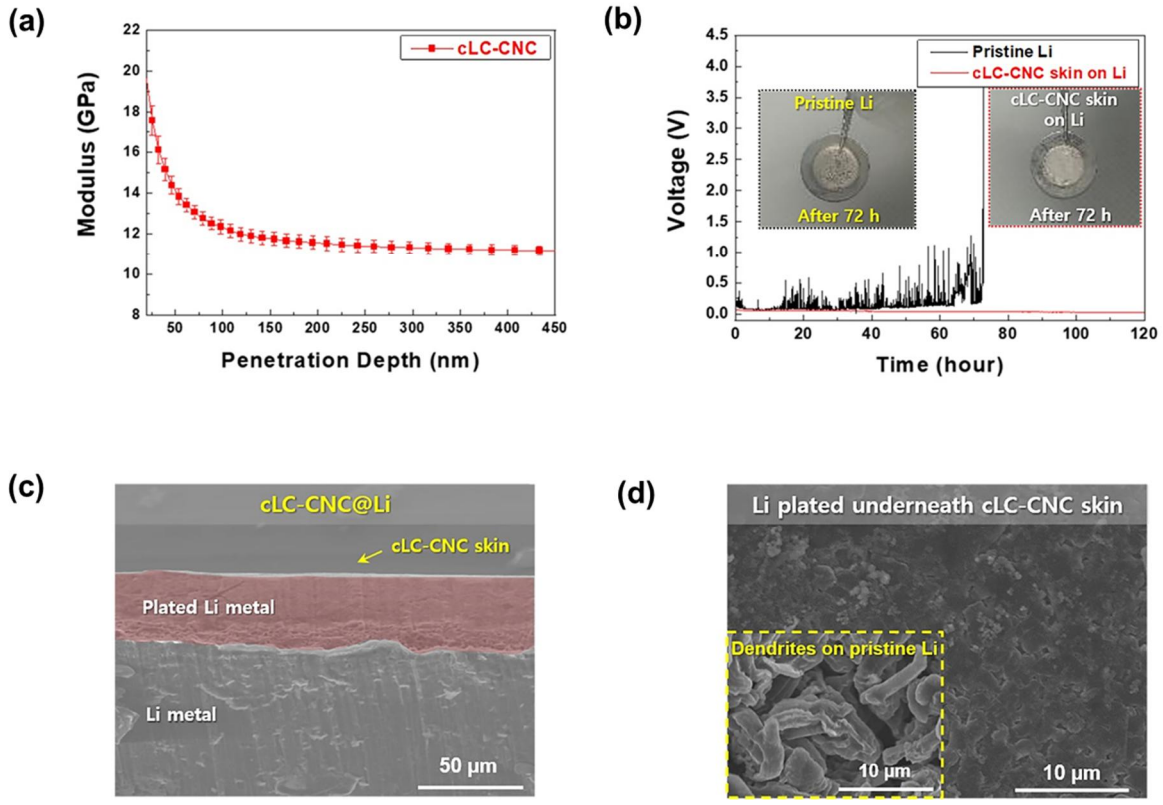

Fig. 30 Suppressing Li dendrite growth by cLC-CNC skin. (a) A plot of the mechanical modulus of the cLC-CNC skin as a function of penetration depth during the nanoindentation test. (b) Unidirectional Li plating profiles (at a current density of 0.35 mA cm^{-2}) and photographs (insets) of the pristine Li and cLC-CNC skin on Li. Morphological characterization of the Li metal with the cLC-CNC skin after the unidirectional Li plating for 72 h: (c) cross-sectional and (d) surface (pristine Li (inset)) SEM images. For the surface analysis, the cLC-CNC skin was pre-removed to exclusively observe the plated Li).

4.3.3 Pitch variation-driven control of the nanoporous structure of cLC-CNC skin

The nanoporous structure of the cLC-CNC skin was precisely tuned by changing its pitch. Pitch, which is defined as the repeating distance required for a complete 360° turn of cLC, is known to

play a vital role in controlling the optical properties of cLC.[32] To successfully use the cLC-CNC skin as an ion-conducting protective layer for Li metal electrodes, tortuosity of the cLC-CNC skin should be tailored to ensure facile ion transport while suppressing the growth of Li dendrites. The pitch of the cLC-CNC skin can be adjusted by varying the sonication time of the CNC suspension.[33,34] By increasing the sonication time, the effective repulsion between the CNCs becomes significant, resulting in longer pitch and a red-shift of the iridescence wavelength. The strong dependence of the pitch on the sonication time is conceptually illustrated in Figure 31a.

Figure 31b shows the cross-sectional morphologies of the cLC-CNC skin as a function of sonication time (0, 1, and 2 h). When sonication was not applied, the pitch was observed to be approximately 238 nm. The pitch increased to higher values (307 nm for 1 h and 337 nm for 2 h, respectively) as the sonication time increased. This result was confirmed by estimating the theoretical pitch values by using Bragg's law that is defined as $\lambda_{max} = n_{avg} P \sin \theta$, where λ_{max} is the maximum reflected wavelength, n_{avg} is the average refractive index, and P is the helical pitch.[26,32,34] In the UV-vis spectra (Figure 31c), a peak reflection was shifted to longer wavelengths (redshifted), corresponding to the pitch increases (λ (0 h) = 369 nm, λ (1 h) = 468 nm, and λ (2 h) = 516 nm). By inserting these values into Bragg's law, we obtained theoretical pitch values: P (0 h) = 239 nm, P (1 h) = 304 nm, and P (2 h) = 331 nm. Notably, these theoretical pitch values match the experimental values well (shown in Figure 31b). The difference in pitch values was verified by measuring the ionic conductivity of the cLC-CNC skin (Figure 31d). Consistent with our initial expectation, the cLC-CNC skin prepared by longer sonication times showed higher ionic conductivity (0.157 (0 h), 0.264 (1 h), and 0.397 (2 h) mS cm^{-1}), indicating the formation of short tortuosity due to the long pitch.

On the basis of this structural characterization of the cLC-CNC skin described above, its effect on the Li plating/stripping behavior was investigated using a Li/Li symmetric cell at a fixed current density of 0.35 mA cm^{-2} and a plating/stripping capacity of 1.75 mAh cm^{-2}. Intriguingly, the cLC-CNC (sonication time = 1 h) showed the best cyclability than the other samples (Figure 31e). The cLC-CNC (0 h) had the lowest ionic conductivity because of longer tortuosity induced by the shorter pitch, thus hindering ion transport that leads to the voltage rise (inset of Figure 31e). Meanwhile, the cLC-CNC (2 h) could cause relatively fast growth of Li dendrites due to the shorter tortuosity, resulting in internal short-circuit failure earlier during the cycling. This plating/stripping result demonstrates that the longstanding trade-off issue of ion transport and dendrite suppression in Li protective layers can be resolved by applying the cLC-CNC.

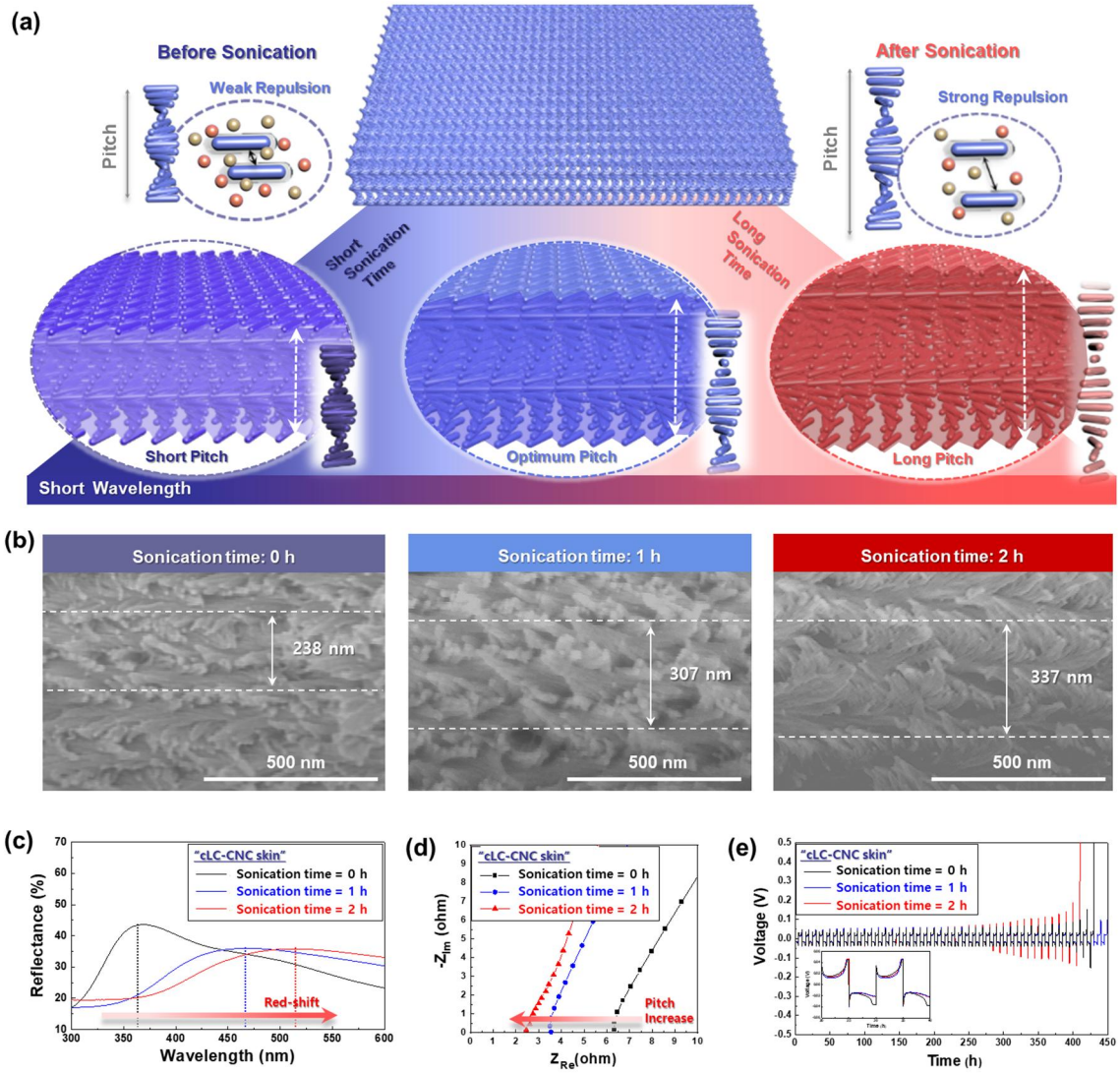

Fig. 31 Control of nanoporous structure of the cLC-CNC layer through pitch variation. (a) Schematic illustration depicting the dependence of pitch on the sonication time. (b)-(d) Structural change of the CNC layers as a function of sonication time (0, 1, and 2 h): (b) Cross-sectional SEM images, (c) UV-vis spectra, (d) Nyquist plots, and (e) Li plating/stripping profiles (at a current density of 0.35 mA cm^{-2} and a plating/stripping capacity of 1.75 mAh cm^{-2}).

4.3.4 Li plating/stripping behavior of cLC-CNC@Li

We investigated the effects of the cLC-CNC skin on the Coulombic efficiency of the Li plating/stripping process using a Li/Cu asymmetric cell, in which the cLC-CNC skin (1 μm)

was deposited on top of a Cu foil (denoted as cLC-CNC@Cu) which served as a working electrode. Figure 32a shows that the Coulombic efficiency of a pristine Cu foil was 92.5% at the 1st cycle under a current density of 0.35 mA cm^{-2} and then sharply decayed after approximately 100 cycles. By comparison, the cLC-CNC skin maintained a high Coulombic efficiency after 150 cycles. The voltage profiles (for the 1st and 120th cycles) of the two samples are shown in Figure 32b-c. This result demonstrates that the cLC-CNC skin can effectively suppress the growth of Li dendrites (which could eventually propagate to form dead Li) owing to its uniform Li ion flux and high mechanical modulus.

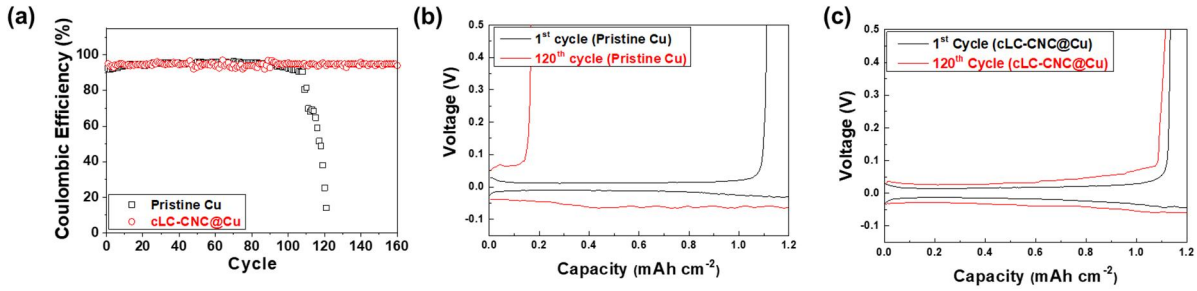

Fig. 32 (a) Coulombic efficiency of the Li/Cu asymmetric cells (pristine Cu vs. cLC-CNC@Cu) at a current density of 0.35 mA cm^{-2} and a plating/stripping capacity of 1.00 mAh cm^{-2}. Voltage profiles of the Li/Cu asymmetric cells ((b) pristine Cu vs. (c) cLC-CNC@Cu) after 1st and 120th cycles.

The Li plating/stripping behavior of Li/Li symmetric cells was investigated on the thin Li metal electrode (20 μm, surface, Figure 33a) with the cLC-CNC skin (denoted as cLC-CNC@Li), in which thin pristine Li metal electrode also was used as a reference. Many previous studies on Li protective layers have employed thick Li electrodes (> 100 μm) and low depth of discharge (DOD < 10%) (Table 2). When the practical use of Li metal anodes for high-energy-density full cells is considered, lower thickness and higher DOD is highly preferred. Figure 33b shows the voltage profiles of the Li/Li symmetric cells at a current density of 0.35 mA cm^{-2} and 30% DOD. The pristine Li had a fluctuating/unstable voltage profile after 420 h, possibly revealing the growth of dendrites, the formation of dead Li, and the continuous consumption of the electrolyte.[7] By contrast, the cLC-CNC@Li exhibited stable cycling retention for 750 h under the same conditions. Moreover, even at a higher DOD (*e.g.*, 50% DOD), superior cycling performance was maintained by the cLC-CNC@Li, whereas the pristine Li lost its electrochemical activity after just 275 h (Figure 34). The advantageous effects of the cLC-CNC skin were verified by examining the morphological changes of the PE separator after the cycling test. For the pristine Li, substantial amounts of filamentary Li dendrites were formed on the

separator facing the Li metal electrode (Figure 35a). The Li dendrites blocked the pores of the separator and hindered ion transport, resulting in the drastic voltage fluctuation. In contrast, the separator in contact with the cLC-CNC@Li was relatively uncontaminated and maintained its pristine porous structure (Figure 35b). We conducted the EIS analysis of the symmetric cells after the cycling tests (Figure 33c). The charge transfer resistance (R_{CT}) of a cell with the pristine Li, which is represented by the semicircle in the Nyquist plot, was larger than that of a cell containing the cLC-CNC@Li. This result indicates the generation of a stable interface in the cLC-CNC@Li, whereas the pristine Li suffers from the formation of a thick SEI layer because of continuous interfacial reactions with the liquid electrolyte.[35] As additional evidence, the cross-sectional morphologies of the Li metals were examined after the cycling tests. The pristine Li had an irregularly formed porous structure composed of needle-like dendrites (Figure 33d), which was consistent with those of previous reports.[27,36] Moreover, the volume expansion of the pristine Li was approximately 450 % (~ 90 μm) relative to the initial value (20 μm before cycling). By comparison, the cLC-CNC@Li had a relatively smooth surface and considerably suppressed volume expansion (~ 190 %, ~ 38 μm) (Figure 33e). Meanwhile, the structural stability of the cLC-CNC skin (cLC-CNC@Li) during the cycling test was investigated using atomic force microscopy (AFM) analysis. The cLC-CNC skin maintained its structural integrity without defects or cracks during the repeated Li plating/stripping cycling (Figure 33f). This result was further verified by observing the polarized optical microscopy image. The cLC-CNC skin retained the activation to polarized light without significant color change that is a salient feature of the cLC structure (Figure 33g), which appeared similar to the result observed before the cycling test. These results underline the advantageous effect of the cLC-CNC skin as an ion-conducting protective layer that can prevent the growth of dendrites and allow uniform Li plating/stripping through the cLC-structured nanoporous channels.

Approaches	Symmetric Cells			References
	Li metal Thickness (μm)	DOD (%)	Cycling Performance (h)	
cLC-CNC Skin	20	30 50	750 400	This Study
Li_2TiO_3 Layer	300	< 2	350	Adv. Energy. Mater. **2019**, 9, 1803722
Organic Polyurea Thin Film	250	< 4	400	Adv. Mater. **2019**, 31, 1806541
Langmuir-Blodgett artificial SEIs	20	< 25	400	Nat. Energy. **2018**, 3, 889-898
Artificial Li_3PO_4 SEI Layer	200	2.5	600	Adv. Mater. **2016**, 28, 1853–1858
Artificial Soft-Rigid LiF/PVdF-HFP Protection Layer	750	0.5	280	Adv. Funct. Mater. **2018**, 28, 1705838
Poly(ethyl α-cyanoacrylate)-Based Artificial SEI Layer	150	3.5	200	Chem. Mater. **2017**, 29, 4682−4689
Artificial TiO_2/lithium n-butoxide hybrid SEI Layer	200 *	2.5	600	Nanoscale. **2019**, 11, 2194-2201
$LiSiO_4$-based Thin Protection Layer	490	< 2.5	200	ACS Appl. Mater. Interfaces **2018**, 10, 8692−8701
Al_2O_3 Coating Layer	450	1	10	Journal of Power Sources, **2015**. 284, 103
Artificial Layer based on LiF through Magnetron Sputtering Deposition	200 *	2.5	165	J. Mater. Chem. A. **2017.** 5, 3483-3492
3D Al_2O_3 Network Artificial Layer	250	-	-	ChemSusChem. **2018**,11, 3243 –3252
ALD coating layer with Al_2O_3	200 *	1	1.7	ACS Nano. **2015**, 9, 5884
Mixed Lithium Oxynitride/Oxysulfide Artificial Layer	260	< 2	250	ACS Appl. Mater. Interfaces. **2018**, 10, 39695−39704
Conformal LiF Protection Layer on Li-rGO	70	6	450	Nano Lett. **2017**, 17, 3731−3737
Antimony-doped Li_3PO_4 SEI Layer	200	2.5	700	ChemElectroChem. **2019**, 6, 1134-1138

Table. 2 Summary of the previous studies on Li protective layers for Li/Li symmetric cells, with focus on Li metal thickness, DOD, and cycling performance.

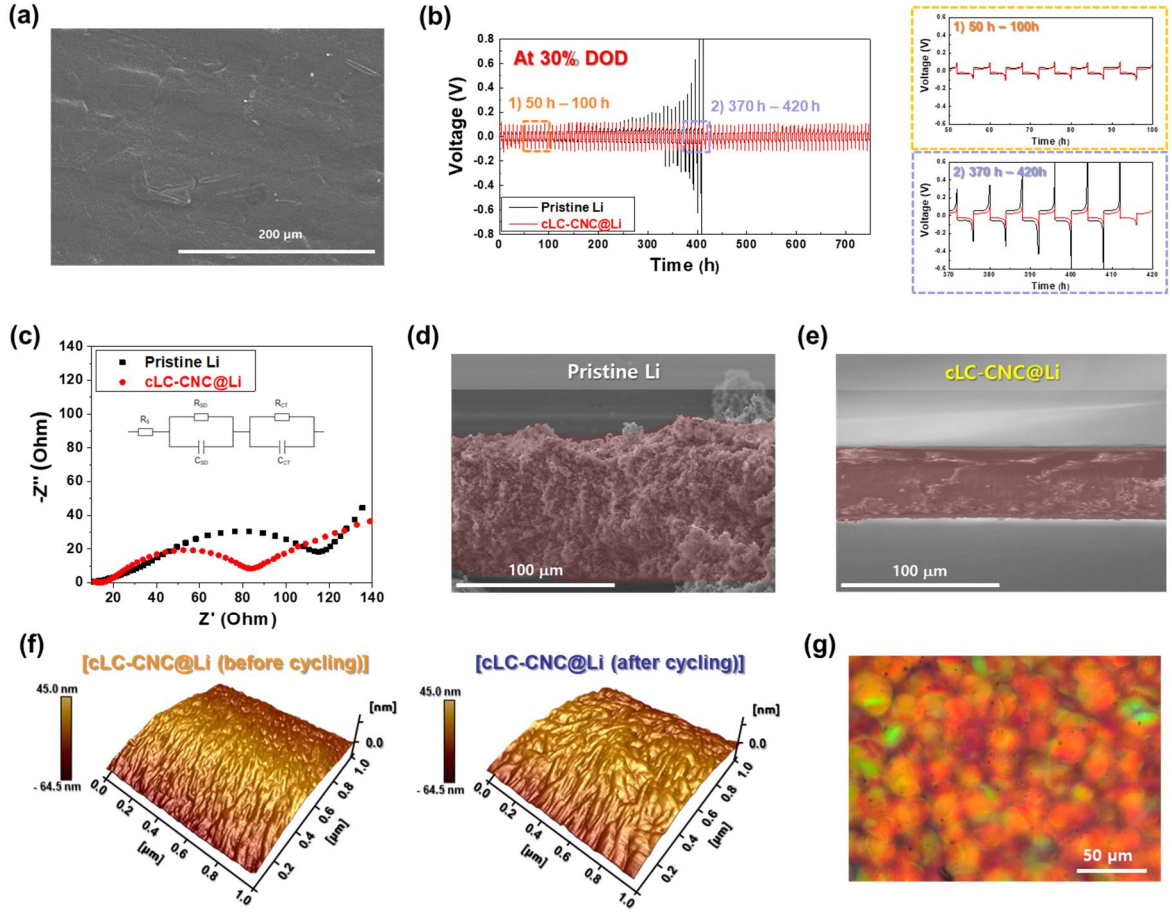

Fig. 33 Effect of the cLC-CNC skin on Li plating/stripping. (a) Cross-sectional SEM image of pristine Li metal on Cu foil. (b) Li plating/stripping profiles (pristine Li vs. cLC-CNC@Li) at a current density of 0.35 mA cm^{-2} and 30 % DOD. (c) EIS analysis of the Li/Li symmetric cells after cycling test (460 h). Cross-sectional SEM images of (d) pristine Li and e) cLC-CNC@Li after the cycling test. (f) AFM images of the cLC-CNC@Li before and after the cycling test. (g) Polarized optical microscopy image of the cLC-CNC skin (cLC-CNC@Li) after the cycling test.

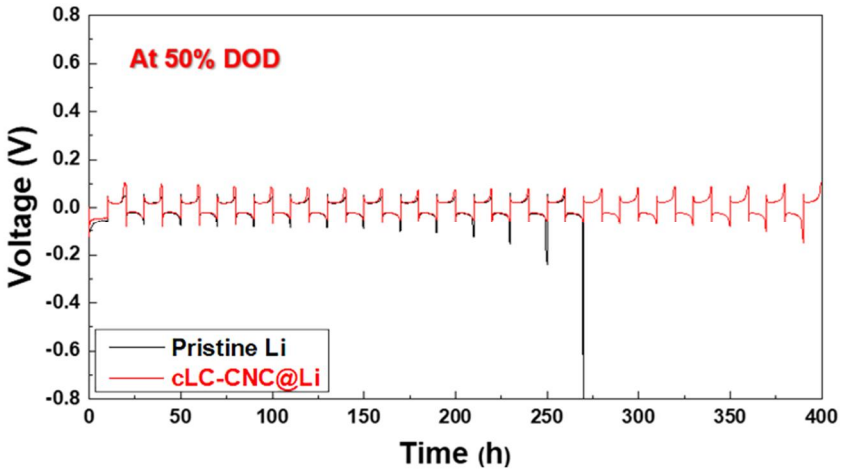

Fig. 34 Li plating/stripping profiles (pristine Li vs. cLC-CNC@Li) at a current density of 0.35 mA cm^{-2} and 50 % DOD.

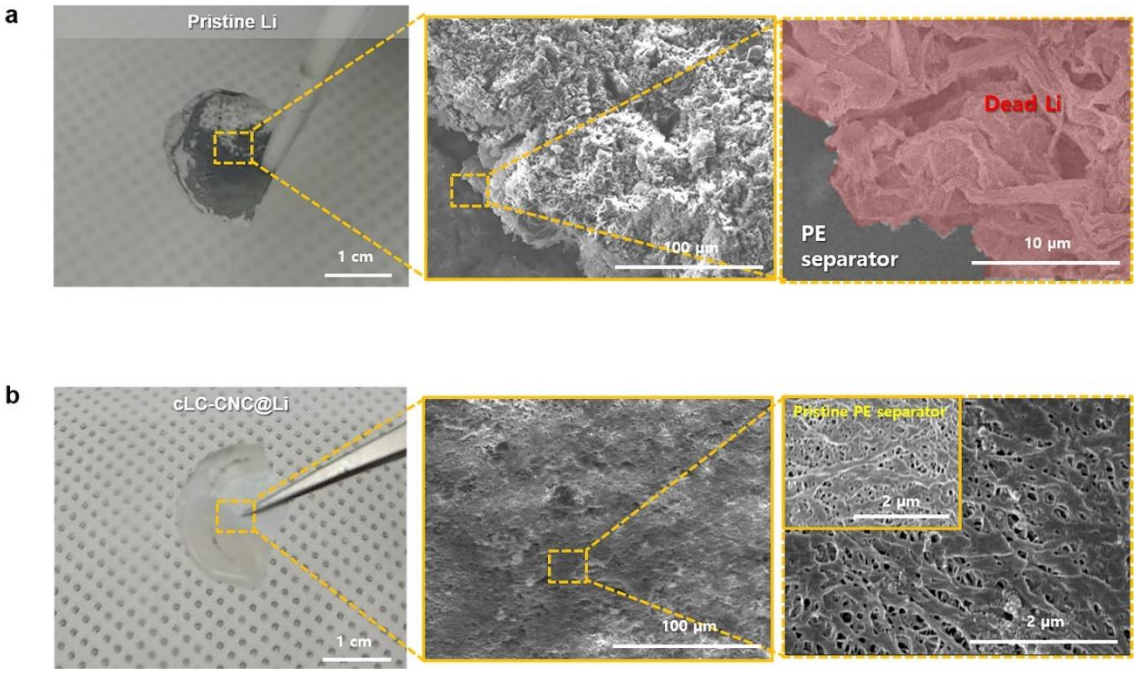

Fig. 35 Photographs and SEM images of the PE separators facing the Li metal anodes after the cycling test (460 h) of symmetric cells: (a) pristine Li vs. (b) cLC-CNC@Li (pristine PE (inset)).

4.3.5 Electrochemical performance of cLC-CNC@Li

We explored the potential use of the cLC-CNC@Li for practical Li metal full cells. To enable practically meaningful high-energy-density Li metal full cells[7,9], a cLC-CNC (1 mm)@Li (20 mm) anode was coupled with a NCM811 cathode (areal capacity = 1.6 and 3.8 mAh cm^{-2}), leading to a capacity excess of the Li metal over the NCM811 (*i.e.*, N (negative electrode capacity)/P (positive electrode capacity)) = 3.5 and 1.5, respectively. Many previous studies on Li protective layers paid little attention to the N/P ratio of Li metal full cells (Table S3). A few reports[10,13,27] showed good cell performance results with low N/P ratios, however, they introduced unusual electrolytes with complex composition ratios and specially designed solvents/salts/additives, which may hinder their versatile use in practical full cells. In this study, when using a commercially accessible conventional electrolyte (1 M $LiPF_6$ in EC/DEC = 1/1 (v/v) with 10 wt.% FEC and 1 wt.% VC), the Li metal full cell with the cLC-CNC@Li showed substantially improved cycling performance (capacity retention = 77% after 200 cycles) at a charge/discharge current density of 0.3 C/0.5 C, in marked contrast to the control full cell with a pristine Li anode (Figure 36a). Furthermore, even under harsher conditions (capacity excess of the Li metal over the NCM811 = 1.5), stable cycling performance was observed in the cLC-CNC@Li anode (capacity retention = 80% after 100 cycles) (Figure 36b), underscoring the beneficial effects of the cLC-CNC skin on the electrochemical performance of Li metal full cells. We anticipate that the absolute values of the cycling retention could be further improved by using high-performance cathodes and electrolytes.

To confirm the superior cycling performance of the cLC-CNC@Li, we examined cross-sectional SEM images of the Li metal anodes after the cycling tests (after 160 cycles). Similar to the results shown in the Li/Li symmetric cells, the thickness of the pristine Li increased considerably (20 → ~ 70 μm) (Figure 36c), revealing the random formation of needle-like Li dendrites.[27,36] By comparison, the thickness increase was suppressed in the cLC-CNC@Li (20 → ~ 32 μm). The thickness increase of the Li metal electrodes during charge/discharge cycling can cause unwanted losses in the volumetric energy density of the Li metal full cells. Considerable attention should be undoubtedly devoted to this issue in order to enable practical Li metal full cells with sustainable electrochemical performance. We investigated the volumetric energy density retention of the Li metal full cells before and after the cycling tests. Figure 36d shows the relationship between the thickness increase of the Li metal and the volumetric cell energy density retention. Due to the suppressed thickness increase, the cLC-CNC@Li exhibited higher volumetric cell energy density retention (92% vs. 70% for the

pristine Li). The significance of the cLC-CNC skin was further highlighted by comparing these results with previous reports on Li protection layers. Most of the previous studies on Li protective layers did not pay serious attention to the change in the thickness of the Li metal electrodes during charge/discharge cycling (Table 3). The advantageous roles of the cLC-CNC as a multifunctional protective layer (*i.e.*, suppressing the Li dendrite growth and the volume expansion of the Li metal electrodes, in addition to allowing facile/uniform Li ion flux) are schematically illustrated in Figure 36e.

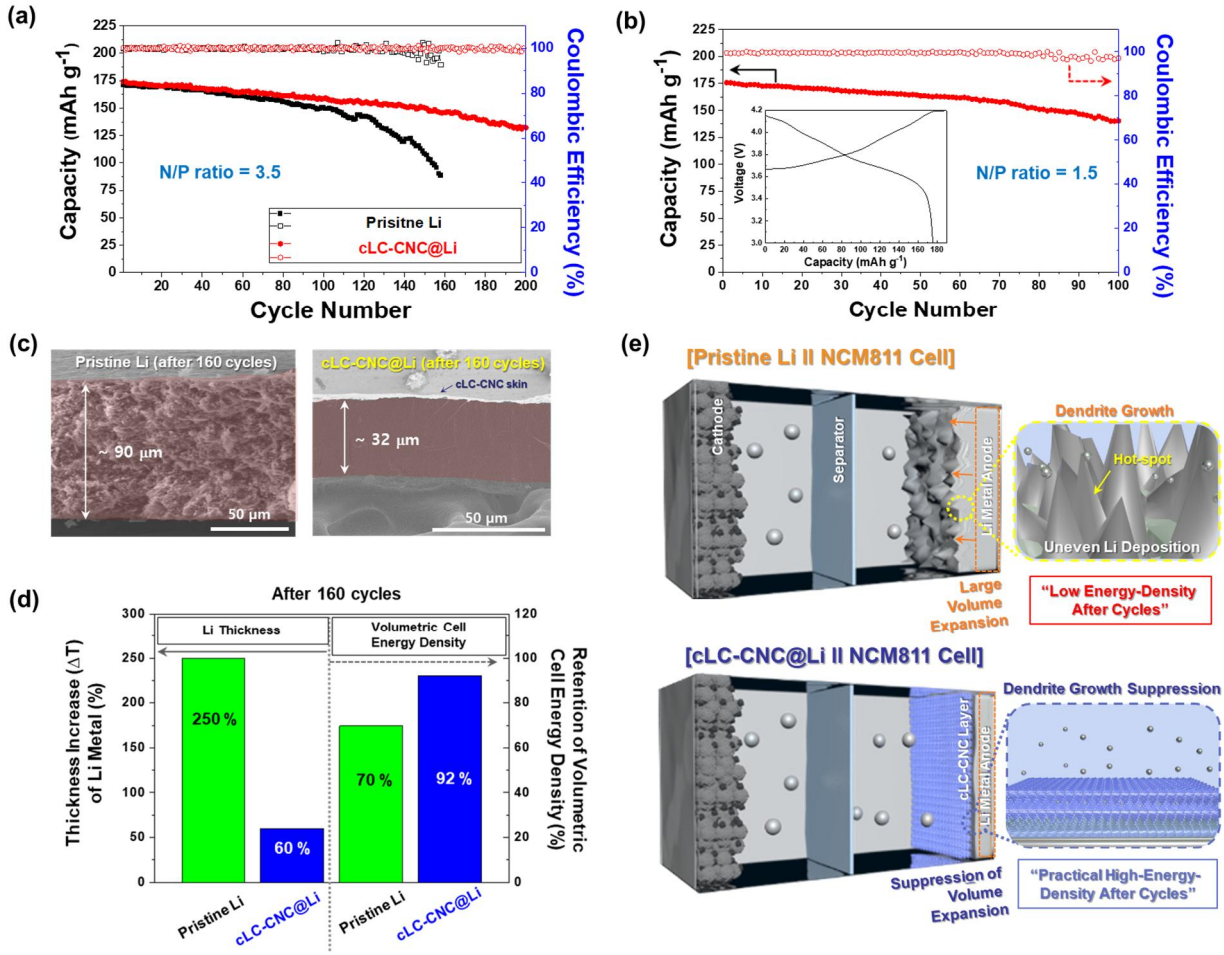

Fig. 36 Potential use of the cLC-CNC@Li for practical Li metal full cells. (a) Cycling performance of the Li metal full cell (composed of cLC-CNC@Li (vs. pristine Li) and NCM811 cathode (areal capacity = 1.6 mAh cm^{-2}, N/P ratio = 3.5) at charge/discharge current densities of 0.3 C/0.5 C. (b) Cycling performance of the Li metal full cell (composed of cLC-CNC@Li and NCM811 cathode (areal capacity = 3.8 mAh cm^{-2}, N/P ratio = 1.5) at charge/discharge current densities of 0.3 C/0.5 C. (c) Cross-sectional SEM images of the pristine Li (left) and cLC-CNC@Li (right) after 160 cycles. (d) Thickness increase

(ΔT) of the Li metals and volumetric cell energy density retention after 160 cycles (pristine Li vs. cLC-CNC@Li). (e) Schematic illustration depicting the advantageous roles of cLC-CNC skin as a multifunctional protective layer for Li metal anodes in full cells.

Approaches	Full Cells					References
	Cathode	Electrolyte	Thickness increase (ΔT) of Li metals after cycling (%)	N/P ratio	Cycling performance (Voltage range)	
CN CNC Protection Layer	NCM811	1.0 M $LiPF_6$ in EC/DEC (1/1, v/v) with 10 wt% FEC and 1wt% VC	60 %	3.5	133 mAh cm^{-2}, 200 cyc (3.0 V-4.2 V)	This Study
				1.5	141 mAh cm^{-2}, 100 cyc (3.0 V-4.2 V)	
Langmuir-Blodgett Artificial SEI	NCM811	0.5M lithium bis(trifluoromethanesulfonyl)imide (LiTFSI, Sigma Aldrich) and 0.5M lithium bis(fluorosulfonyl)imide (LiFSI, Lichem) in fluoroethylene carbonate (FEC, PanaX Etech):dimethyl carbonate (DMC, PanaX Etech) by 3:7 volume ratio		Half Cell	~ 131 mAh g^{-1}, 250 cyc (2.7 V-4.3 V)	Nat. Energy. **2018**, 3, 889-898
		0.6 M LiTFSI, 0.4 M LiBOB, 0.4 M lithium fluoride (LiF), 0.1 M lithium nitrate ($LiNO_3$), 0.05 M $LiPF_6$ and 0.03 M lithium tetrafluoroborate ($LiBF_4$) in EC:DMC (2/1, v/v) with 1 wt% FEC and 2 wt% VC and 3 wt% di-2,2,2-trifluoroethyl carbonate (TFEC)		2.5	155 mAh g^{-1}, 330 cyc (2.7 V-4.3 V)	
				1.0	~ 155 mAh g^{-1}, 200 cyc (2.7 V-4.3 V)	
Li_2TiO_3 Layer	NCM811	1.3 M $LiPF_6$ in EC/DEC (3/7, v/v) with 10wt% FEC	-	Half Cell	125 mAh g^{-1}, 500 cyc (2.8 V- 4.2 V)	Adv. Energy. Mater. **2019**, 9, 1803722
Organic Polyurea Thin Film	LFP	1.0 M $LiPF_6$ in EC/DEC/DMC (1/1/1, v/v/v)	-	Half Cell	120 mAh g^{-1}, 200 cyc (2.8 V- 4.2 V)	Adv. Mater. **2019**, 31, 1806541
Artificial Li_3PO_4 SEI Layer		1.0 M $LiPF_6$ in EC/DEC/DMC (1/1/1, v/v/v)	-	Half Cell	140 mAh g^{-1}, 200 cyc (2.2 V- 4.2 V)	Adv. Mater. **2016**, 28, 1853–1858
Artificial Soft-Rigid LiF/PVdF-HFP Protection Layer		1.0 M $LiPF_6$ in EC/DEC (1/1, v/v)	-	Half Cell	120 mAh g^{-1}, 250 cyc (2.5 V- 4.2 V)	Adv. Funct. Mater. **2018**, 28, 1705838
Poly(ethyl α-cyanoacrylate)-Based Artificial SEI Layer		1.0 M $LiPF_6$ in EC/DMC (1/1, v/v)	-	Half Cell	135 mAh g^{-1}, 500 cyc (2.7 V- 4.0 V)	Chem. Mater. **2017**, 29, 4682−4689
Artificial TiO_2/lithium n-butoxide hybrid SEI Layer		1.0 M $LiPF_6$ in EC/DMC/EMC (1/1/1, v/v/v) with 1% VC	-	Half Cell	140 mAh g^{-1}, 200 cyc (2.0 V- 4.0 V)	Nanoscale. **2019**, 11, 2194-2201
$LiSiO_4$-based Thin Protection Layer		1.0 M LiTFSI in dioxolane (DOL)/dimethoxyethane (1/1, v/v) with 0.2 M $LiNO_3$	-	Half Cell	100 mAh g^{-1}, 100 cyc (1.7 V- 2.8 V)	ACS Appl. Mater. Interfaces **2018**, 10, 8692−8701
Poly(vinylidene difluoride) Coating Protection Layer		1.2 M $LiPF_6$ in EC/DMC with 4 wt% FEC (1/2, v/v)	-	Half Cell	140 mAh g^{-1}, 200 cyc (2.5 V- 3.8 V)	Adv. Energy Mater. **2018**, 8, 1701482
Al_2O_3 Coating Layer	LCO	1.0 M $LiClO_4$ in EC/PC (1/1, v/v)	-	Half Cell	1.5 mAh, 400 cyc (3.0 V- 4.2 V)	Journal of Power Sources, **2015**. 284, 103
Artificial Layer based on LiF through Magnetron Sputtering Deposition	LTO	1.0 M $LiPF_6$ in EC/DEC (1/1, v/v)	-	Half Cell	135 mAh g^{-1}, 500 cyc (2.8 V- 4.2 V)	J. Mater. Chem. A. **2017**. 5, 3483-3492
Artificial Li_3N SEI layer		1.0 M $LiPF_6$ in EC/DEC (1/1, v/v) with 1 vol% VC	-	4.5	125 mAh g^{-1}, 100 cyc (1.0 V- 3.0 V)	Adv. Mater. **2017**, 29, 1605531
3D Al_2O_3 Network Artificial Layer	NCM111	1.0 M $LiPF_6$ in EC/DMC/EMC (1/1/1, v/v/v)	-	Half Cell	100 mAh g^{-1}, 120 cyc (3.0 V- 4.3 V)	ChemSusChem. **2018**,11, 3243 –3252
Mixed Lithium Oxynitride/Oxysulfide Artificial Layer	Sulfur	1.0 M LiTFSI in DOL/DME (1/1, v/v) with 0.4 M $LiNO_3$	-	Half Cell	840 mAh g^{-1}, 300 cyc (1.7 V- 2.8 V)	ACS Appl. Mater. Interfaces. **2018**, 10, 39695−39704
Double-layer Diamond Film		1.0 M LiTFSI in DOL/DME (1/1, v/v) with 5 M Li_2S_8	-	3.1	600 mAh g^{-1}, 400 cyc (1.7 V- 2.8 V)	Joule. **2018**, 2, 1595-1609
Conformal LiF Protection Layer on Li-rGO		1.0 M LiTFSI in DOL/DME (1/1, v/v) with 1% $LiNO_3$	-	6.0	1000 mAh g^{-1}, 100 cyc (1.7 V- 2.6 V)	Nano Lett. **2017**, 17, 3731−3737

Table. 3 Summary of the previous studies on Li protective layers for Li metal full cells, with focus on thickness change (ΔT) of Li metals before/after cycling test, electrolyte chemistry, N/P ratio, and cycling performance.

4.4 Conclusion

In summary, we have demonstrated the cLC-CNC skin as a new concept of ion-conducting protective layers for sustainable Li metal electrodes. The cLC structure and the variation in the pitch of the cLC-CNC skin were elaborately tuned, with particular focus on their effects on ion transport tortuosity and dendrite suppression. Due to the well-defined cLC structure and the high mechanical modulus of CNCs, the cLC-CNC skin allowed uniform Li ion flux and improved the Li plating/stripping cyclability, while simultaneously preventing the Li dendrite growth and alleviating the volume expansion of Li metal electrodes. The cLC-CNC@Li was coupled with a high-capacity NCM811 cathode to develop a practical high-energy-density Li metal full cell. The resulting Li metal full cell showed higher cycling performance than the control full cell containing a pristine Li metal anode. Notably, the thickness change of the Li metal during charge/discharge cycling was suppressed in the cLC-CNC@Li, resulting in the superior volumetric cell energy density retention. We envision that the cLC-CNC skin, which is difficult to attain with traditional synthetic materials, holds great promise as a natural material platform that can bring new opportunities for development of next-generation metal battery electrodes.

4.5 References

1. A. Majumdar et al., *Nature*, **2012**, 488, 294-303.
2. J.-G. Zhang et al., *Energy Environ. Sci*., **2014**, 7, 513-537.
3. J.-G. Zhang et al., *Nat. Energy*, **2019**, 4, 180-186.
4. L. A. Archer et al., *Nat. Energy*, **2016**, 1, 1-7.
5. A. Newman et al., *Nat. Energy*, **2018**, 3, 16-21.
6. Y. S. Meng et al., *Nature*, **2019**, 572, 511-515.
7. D. Lin, Y. Liu and Y. Cui et al., *Nat. Nanotech*., **2017**, 12, 194-206.
8. K. Xu et al., *Energy Environ. Sci*., **2019**, 12, 780-794.
9. W. Xu et al., *Adv. Energy Mater*., **2018**, 8, 1703022.
10. Y. Cui et al., *Adv. Mater*., **2017**, 29, 1605531.
11. Q. Qiao, *Nat. Commun*, **2020**, 11, 1-10.
12. M. Noked, *ACS Nano*, **2015**, 9, 5884-5892.
13. Y. Cui et al., *Joule*, **2018**, 2, 1595-1609.
14. W. Choi, *Nat. Nanotech.,* **2018**, 13, 337-344.
15. B. Wei, *Nano Lett*, **2018**, 18, 2067-2073.
16. W. Liu, D. Lin, A. Pei and Y. Cui, *J. Am. Chem. Soc*., **2016**, 138, 15443-15450.
17. H. Zhang et al., *Nat. Commun*, **2018**, 9, 3729.
18. S. Sun et al., *Nat. Commun*, **2020**, 11, 643.
19. D. Wang et al., *Nat. Energy*, **2018**, 3, 1076-1083.
20. Y. Cui et al., *Nat. Commun*, **2016**, 7, 10992.
21. O. J. Roja et al., *Chem. Rev*., **2010**, 110, 3479-3500.
22. S. Y. Lee et al., *Adv. Mater*., **2019**, 31, 1804826.
23. M. J. MacLachlan et al., *Nature*, **2010**, 468, 422-425.
24. J. Zhang et al., *Biomacromolecules*, **2014**, 15, 4343-4350.
25. J. Majoinen, E. Kontturi, O. Ikkala and D. G. Gray, *Cellulose,* 2012, **19**, 1599-1605.
26. S. Vignolini et al., *ACS. Appl. Mater. Interfaces*., **2014**, 6, 12302-12306.
27. W. Il Cho et al., *Nat. Energy*, **2018**, 3, 889-898.
28. S.-Y. Lee et al., *Energy Environ. Sci*., **2019**, 12, 177-186.
29. S. Y. Lee et al., *Adv. Funct. Mater.,* **2020**, 30, 1908868.
30. L. A. Archer et al., *Nat. Commun*, **2015**, 6, 10101.
31. Y. G. Guo et al., *Adv. Mater*., **2016**, 28, 1853-1858.
32. M. J. MacLachlan et al., *Angew. Chem., Int. Ed*., **2015**, 54, 2888-2910.
33. Q. Wu et al., *Biomacromolecules*, **2013**, 14, 1529-1540.
34. R. Berry et al., *Biomacromolecules*, **2011**, 12, 167-172.
35. W. Xu et al., *Adv. Energy Mater*., **2016**, 6, 1502151.

36. J.-G. Zhang, *Adv. Funct. Mater.,* **2017**, 27, 1704391.

Chapter . Electrodes-customized Functional Separators for Lithium-Metal Battery

5.1 Introduction

The forthcoming ubiquitous electronics era, which will find widespread use of the Internet of Things, flexible/wearable devices, and electric vehicles, has led to the pursuit of high-energy-density power sources with electrochemical sustainability.[1,2] Among the numerous power sources reported to date, lithium-ion batteries (LIBs) have been widely used in various applications. However, LIBs are still struggling to meet the continuously increasing demand for high-energy-density applications. Li metal electrodes have recently garnered considerable attention as a promising material approach to resolve this issue, because of their low weight, low electrode potential (-3.04 V vs. standard hydrogen electrode), low density (0.534 g cm^{-3}), and high theoretical capacity (3860 mAh g^{-1}).[3-5] Also, to maximize the energy density of Lithium metal battery, the cathode should be considered. Recently, the high-Ni active materials, which has the high voltage and capacity, has been used as cathode for high energy density.

Despite having such enormous potential, Li metal electrodes are still away from practical use due to their interfacial instability with electrolytes, formation of Li dendrites, uncontrolled volume changes, and generation of electrically inactive "dead Li".[6] These challenges have forced the use of thick Li metal electrodes (> 100 μm) with low utilization (< 10 %), resulting in serious losses of cell energy density.[7,8] The cathode are struggling with dissolution of heavy metal ions (such as Mn and Ni ions) from cathode to anode. This leads to the capacity fading during cycling.

Considering the limitations of current state, the new design of separator is required. Here, we present the new class of electrodes-customized functional separator for resolving the issues of cathode and anode. In anode side, to stabilize the Li metal anode, the functional paper separator based on cellulose nanofiber (CNF) with anion-trapping ability for high Li transference number was introduced. In cathode side, to suppress the heavy-metal ion dissolution (Mn^{2+} ions), the functional paper separator based on CNF with metal chelating was used. Through these functionalities optimized for each electrode, the functional nanocellulose-based bi-layer paper separator can improve the performance of Li metal battery.

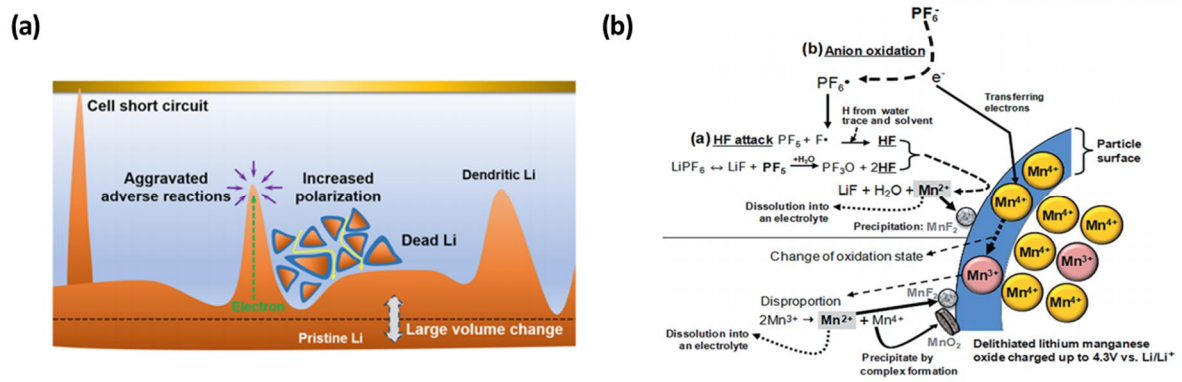

Fig. 37 Issues of (a) Li metal anode (formation of dead Li and dendrites) and (b) High-Ni cathode (dissolution of heavy metal ions). (*Chem. Rev.* 2017, 117, 10403, *RSC Adv.*, 2015, 5, 2732) Copyright © 2017 and 2015 Royal Society of Chemistry.

5.2 Results and Discussion

5.2.1 Characterizations of nanocellulose for anode (N-A)

The nanocellulose for anode (N-A) was synthesized with functional group as quaternary ammonium group for trapping the anions in electrolyte, leading to high Li ion transference number. Through synthesis steps, the N-A was developed. To confirm the existence of functional group, the several characterizations were conducted. Due to the cationic group of N-A, the zeta-potential of N-A showed higher positive value (+ 40.0 mV) than pristine CNF (- 23.0 mV). Also, the nitrogen of quaternary ammonium group was observed through the results of FT-IR and XPS. It indicates that the cationic functional group of N-A was successfully substituted.

(a)

Samples	Zeta-potential (mV)
Pristine CNF	- 23.0
Nanocellulose for anode (N-A)	+ 40.0

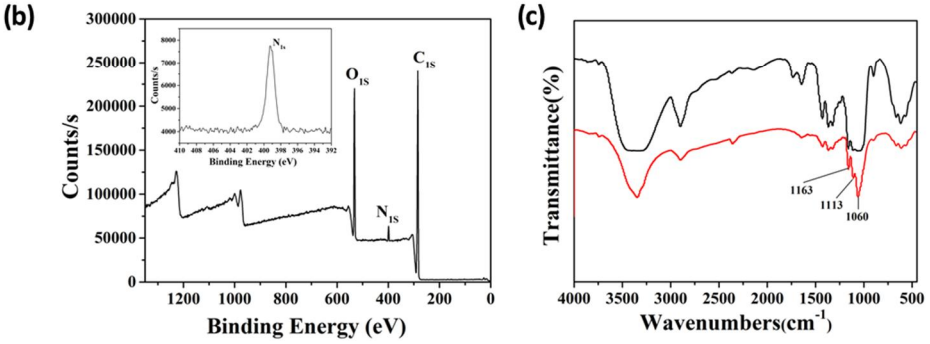

Fig. 38 Characterizations of functional groups on N-A: Results of (a) zeta-potential, (b) XPS and (c) FT-IR.

5.2.2 Characterizations of nanocellulose for cathode (N-C)

The nanocellulose for cathode (N-C) was synthesized with functional group as thiol group (-SH) for chelating the heavy metal ions from cathode, leading to suppression of heavy metal ion transport to Li metal anode. Through synthesis steps, the N-C was developed. To confirm the existence of functional group, the several characterizations were conducted. Due to the thiol group of N-C, the zeta-potential of N-C showed higher negative value (- 32.0 mV) than pristine CNF (- 23.0 mV). Also, the thiol group was observed through the results of FT-IR, indicating that the functional group of N-C was successfully substituted.

(a)

Sample	Zeta-potential (mV)
Pristine CNF	- 23.0
CNF for Cathode (N-C)	- 32.0

(b)

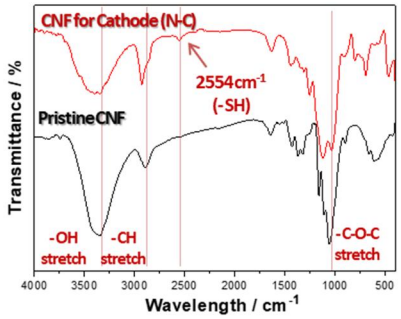

Fig. 39 Characterizations of functional groups on N-C: Results of (a) zeta-potential, (b) FT-IR.

5.2.3 Functional performance of N-A separator

The N-A and N-C separator were fabricated through vacuum filtration. To enlarge the pore-size of separator, the freeze-drying method was introduced. Before applying to separator, the ionic conductivity of fabricated N-A separator was explored. N-A separator showed the lower resistance than PE separator, due to their well-developed web-like nanoporous structure.

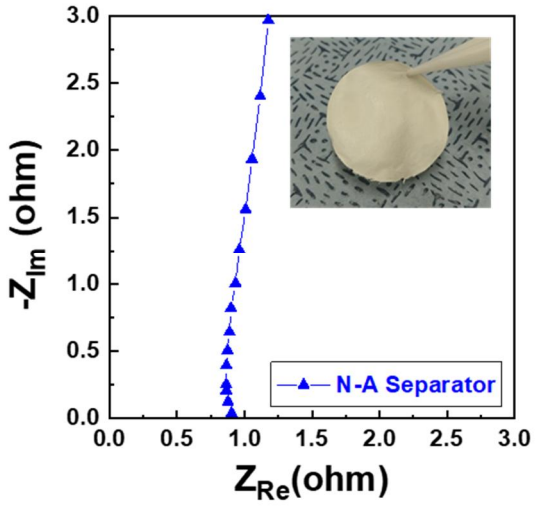

Fig. 40 Ionic conductivity of N-A separator.

To explore the feasibility of the N-A separator as single-ion conducting separator for Li metal electrodes, we conducted a Li/Li symmetric cell test, in which Li plating/stripping cycling was performed using a conventional carbonate-based liquid electrolyte (1 M $LiPF_6$ in EC/DEC = 1/1 (v/v) with 10 wt.% FEC and 1 wt.% VC) at a fixed current density of 0.5 and 3.0 mA cm^{-2} with 1.0 mAh cm^{-2} (Figure 41). The nanoporous structure was confirmed by identifying its nanoporous channels. The N-A separator had stable Li plating/stripping cyclability along with low polarization, compared to the pristine control sample. This result demonstrates that the N-A separator, due to its well-defined nanoporous structure and anion-trapping effect, allows uniform and homogeneous ion flux toward the Li metal and prevents random growth of Li dendrites.

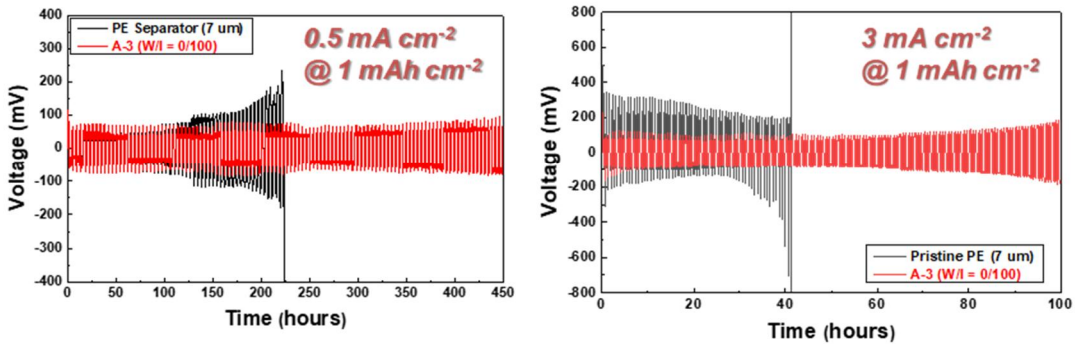

Fig. 41 Li/Li symmetric cell performance of N-A separator.

5.2.4 Functional performance of N-C separator

To explore the feasibility of the N-C separator as heavy metal chelating separator for cathode, we conducted an ionic conductivity and metal chelating ability of N-C separator. N-C separator showed the lower resistance than PE separator, due to their well-developed web-like nanoporous structure and high wettability (Figure 42a). To confirm the chelating ability of N-C separator, the N-C separator was immersed in 10 mM $(MnClO_4)_2$ in electrolyte for 2 hours. After rinsing, captured Mn^{2+} ions were measured through ICP-MS. The N-C separator exhibited high contents of Mn ion, indicating the superior capturing ability of N-C separator derived from chelating group (Figure 42b).

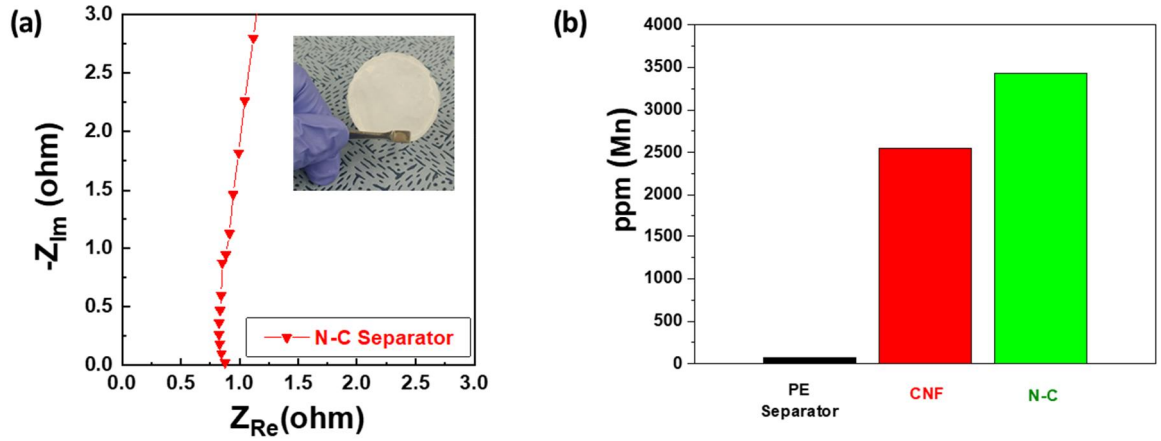

Fig. 42 (a) Ionic conductivity and (b) captured amounts of Mn ion through ICP-MS.

5.2.5 Electrochemical performance of bi-layer separator (N-A@N-C separator)

We explored the potential use of the functional paper bi-layer separator (N-A@N-C separator) for practical Li metal full cells. To enable practically meaningful high-energy-density Li metal full cells, Li (20 μm) anode was coupled with Over-lithiated layer oxide ($0.33Li_2MnO_3$•$0.67LiNi_{0.18}Mn_{0.65}O_2$), leading to a capacity excess of the Li metal (*i.e.*, N (negative electrode capacity)/P (positive electrode capacity)) = 3.5). In this study, when using a commercially accessible conventional electrolyte (1 M $LiPF_6$ in EC/DEC = 1/1 (v/v) with 10 wt.% FEC and 1 wt.% VC), the Li metal full cell with the paper cathode and bi-layer separator showed substantially improved cycling performance at a charge/discharge current density of 1.0 C/1.0 C, in marked contrast to the control full cell with a pristine Li anode (Figure 43). We anticipate that the absolute values of the cycling retention could be further improved by using high performance electrolytes.

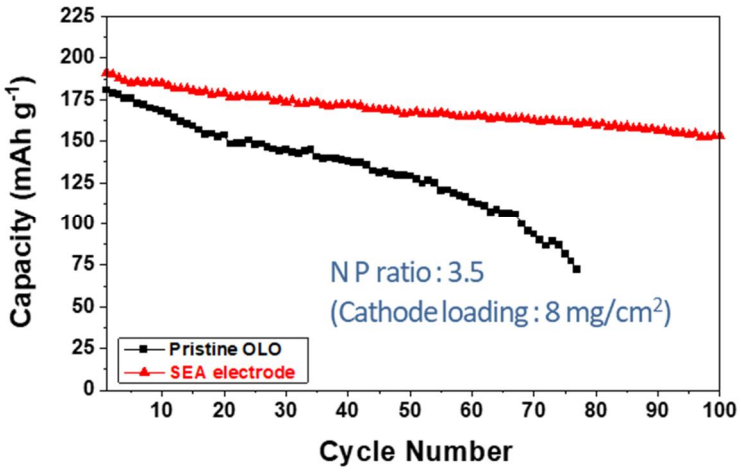

Fig. 43 Cycling performance of the Li metal full cell (composed of paper cathode and bi-layer separator (vs. pristine Li), N/P ratio = 3.5) at charge/discharge current densities of 1.0 C/1.0 C.

5.3 References

1. A. Majumdar et al., *Nature*, **2012**, 488, 294-303.
2. J.-G. Zhang et al., *Energy Environ. Sci*., **2014**, 7, 513-537.
3. J.-G. Zhang et al., *Nat. Energy*, **2019**, 4, 180-186.
4. L. A. Archer et al., *Nat. Energy*, **2016**, 1, 1-7.
5. A. Newman et al., *Nat. Energy*, **2018**, 3, 16-21.
6. Y. S. Meng et al., *Nature*, **2019**, 572, 511-515.
7. D. Lin, Y. Liu and Y. Cui et al., *Nat. Nanotech*., **2017**, 12, 194-206.
8. K. Xu et al., *Energy Environ. Sci*., **2019**, 12, 780-794.

List of Publications

(First author)

- Y.-H. Lee, S.-Y. Lee*, "Electrodes-customized multifunctional paper separator and electrode" (*Manuscript Preparation*)

- K.-S. Oh, Y.-H. Lee, S.-Y. Lee*, "Overlooked organic/inorganic hybrid electrolyte design" (*Manuscript Preparation*)

- Y.-H. Lee, C.-D. Lee, J. –H. Kim, J. –Y. Seo, S. –W. Kim, W. –J. Youe, J. –G. Gwon, S.-Y. Lee*, S.-Y. Lee*, "Cholesteric liquid crystalline cellulose nanocrystal skin for sustainable lithium metal electrodes." (*Submission*)

- Y.-H. Lee+, Z. Wang+, S.-W. Kim, J. –Y. Seo, S.-Y. Lee*, "Why Cellulose Based Electrochemical Energy Storage Devices?."
Adv. Mater. 2000892 (2020)

- D.-H. Kim+, Y.-H. Lee+, Y.-B. Song, H.-R. Kwak, S.-Y. Lee*, Y. S. Jung*, "Thin and Flexible Solid Electrolyte Membranes with Ultrahigh Thermal Stability Derived from Solution-Processable Li Argyrodites for All-Solid-State Li-Ion Batteries." *ACS Energy Lett.* 5, 718-727 (2020)

- Y.-H. Lee, J. –H. Kim, J.-H. Kim, J. –T. Yoo, S.-Y. Lee*, "Spiderweb Mimicking Anion Exchanging Separators for Li–S Batteries."
Adv. Funct. Mater. 28, 1801422 (2018) [Front Cover Image]

- J.-H. Kim+, G.-Y. Jung+, Y.-H. Lee +, J. -H. Kim, S. Y. Lee, S.-Y. Lee*, "Polysulfide-Breathing/Dual-Conductive, Heterolayered Battery Separator Membranes Based on 0D/1D Mingled Nanomaterial Composite Mats" *Nano Lett.* 17, 2220 (2017)

(Co-author)

- S.-H. Hong, D. -H. Jung, J.-H. kim, Y. -H. Lee, S. –J. Cho, S. H. Joo, H. –W. Lee*, K. –S. Lee*, S.-Y. Lee*, *Adv. Funct. Mater.* 1908868 (2020)

- C. M. Costa, Y.-H. Lee, J. –H. Kim, S.-Y. Lee*, S. L. Mendez, "Recent advances on separator membranes for lithium-ion battery applications: from porous membranes to solid electrolytes." *Energy Storage Mater.* (2019)

- J.-H. Kim, Y.-H. Lee, S.-J. Cho, J.-G. Gwon, H.-J. Cho, M. Jang, S.-Y. Lee*, S.-Y. Lee*, Energy Environ. Sci. 12, 177 (2019)

- J.-H. Kim, D. –G. Lee, Y.-H. Lee, W. Chen, S.-Y. Lee*, *Adv. Mater.* 25, 6029 (2019)

- S.-J. Cho, K. -H. Choi, J.-T. Yoo, J.-H. Kim, Y. -H. Lee, S. -J. Chun, S. –B. Park, D. –H. Choi, Q., S.-Y. Lee*
Adv. Funct. Mater. 25, 6029 (2015)

Acknowledgements

It was a wonderful journey to complete Ph.D program here in UNIST, full of passion, curiosity and excitement. For several years of study, Prof. Sang-Young Lee and Hyun-Wook lee has led me to learn science and technology but also life. I would like to express my deep gratitude to advisor for his constant support, inspirational guidance and academic feedback. It was a great pleasure to meet many insightful scholars at UNIST including my thesis committee members.

I would like to acknowledge and give thanks to my colleagues, collaborators, Dr. Dong Hyeon Kim and Jae-Gyung Gwon for their passionate and dedicated contribution. I really thank for many members including my membrane team members, Dr. Jung-Hwan Kim, Dr. Se-Hee Kim, Dr. Ju-Myung Kim, Jeong-Hoon Kim, Yeon-Su Oh, Sang-Ho Hong, Sang-Woo Kim, Ji-Young Seo and Young-Guk Hong. Additionally, during degree period, I would like to thank my friend Jung-Won Kim, teacher Sung-Min Jung and members of youth group in Sungil for helping me a lot when suffering hard time. Thanks for always being supportive in all the situations I faced during the years of my Ph.D studies. I think no one can destroy our unique relationships.

Most of all, I would like to appreciate to my family. I have no doubt that I accomplish the research achievements with their support and sacrifice. Also, I would like to thank Emily Won who has always been supportive and given me confidence. Without their assistance and understanding, it would have never been possible for me to accomplish this achievement. Thank you all.